Atmos. Chem. Phys., 26, 8961–8979, 2026
https://doi.org/10.5194/acp-26-8961-2026

Atmospheric Chemistry and Physics
Open Access
EGU

What caused record-breaking aerosol loading over the South China Sea in April 2023

Saginela Ravindra Babu[1] **and Neng-Huei Lin**[1,2]

[1]Department of Atmospheric Sciences, National Central University, Taoyuan 32001, Taiwan
[2]Center for Environmental Monitoring and Technology, National Central University, Taoyuan 32001, Taiwan

Correspondence: Saginela Ravindra Babu (baburavindra595@gmail.com) and Neng-Huei Lin (nhlin@cc.ncu.edu.tw)

Received: 28 August 2025 – Discussion started: 4 September 2025
Revised: 26 May 2026 – Accepted: 11 June 2026 – Published: 25 June 2026

Abstract. In April 2023, record-breaking aerosol optical depth (AOD) levels were observed over the South China Sea (SCS). This study investigates the sources, transport pathways, and large-scale dynamical conditions associated with this extreme aerosol event. Observations from the Moderate Resolution Imaging Spectroradiometer (MODIS) revealed the highest April AOD in the 2003–2023 satellite record, with values increasing by approximately 150 % relative to the 2003–2022 climatological mean and exceeding 4σ above normal conditions. Enhanced carbon monoxide (CO) concentrations were simultaneously detected in the free to mid-troposphere (700–500 hPa) by Measurements of Pollution in the Troposphere (MOPITT) and Atmospheric Infrared Sounder (AIRS), indicating substantial long-range transport of combustion-related pollution. MODIS fire count and burned-area datasets further indicated intensified biomass-burning (BB) activity over northern Peninsular Southeast Asia (PSEA) during the same period. Backward trajectory simulations using the NOAA Hybrid Single-Particle Lagrangian Integrated Trajectory (HYSPLIT) model suggested that a large fraction of air masses arriving over the SCS originated from northern PSEA, supporting the interpretation that BB emissions from this region contributed substantially to the elevated aerosol loading over the SCS. Dynamical analyses revealed a persistent anti-cyclonic anomaly over northern PSEA at 500 hPa, accompanied by an eastward-shifted Bay of Bengal anticyclone at 700 hPa and a western North Pacific cyclonic anomaly at both levels. These circulation anomalies likely altered the prevailing regional flow by shifting climatological southerlies toward northerly anomalies, thereby favoring aerosol transport and accumulation over the SCS. Overall, the results suggest that the extreme aerosol event was associated with the combined influence of intensified BB emissions and anomalous atmospheric circulation, highlighting the important role of coupled emissions and atmospheric dynamics in shaping regional aerosol extremes.

1 Introduction

Atmospheric aerosols play a vital role in Earth's climate by impacting radiation balance, cloud microphysics, and air quality (Ramanathan et al., 2001; Anderson et al., 2003; Forster et al., 2021; IPCC, 2023). These particles scatter and absorb solar radiation directly, influencing radiative effects, and also modify cloud properties, lifespan, and precipitation by serving as nuclei for condensation and ice formation. As a result, aerosols affect atmospheric thermodynamics, cloud–radiation interactions, and the water cycle (Twomey, 1977; IPCC, 2023). Monitoring aerosol levels over remote ocean regions is especially important because these areas provide a baseline for natural background aerosol levels and help evaluate the effects of long-range transport on regional climate through radiative and cloud processes (Pani et al., 2023). In addition to anthropogenic emissions, natural events such as wildfires and agricultural biomass-burning (BB) are significant episodic sources, emitting large quantities of aerosol particles and trace gases that substantially affect both regional and global climate systems (Crutzen and Andreae,

1990; Ramanathan et al., 2001; Lin et al., 2013; Reid et al., 2013; Kolden et al., 2024).

The South China Sea (SCS), situated in Asia, is the largest marginal sea in the tropical–subtropical western North Pacific (WNP), serving as a vital natural laboratory for examining aerosol variability in a relatively pristine marine environment (Reid et al., 2013; Lin et al., 2013; Pani et al., 2023). Although it is an oceanic region, the atmosphere over the SCS is significantly influenced by emissions from nearby continents and regional circulation patterns (Pani et al., 2023). Typically, the SCS is dominated by a monsoon system, with the northeast monsoon occurring during boreal winter and spring, and the southwest monsoon during boreal summer and autumn (Cui et al., 2016). These seasonal wind patterns play a key role in aerosol transport, often carrying natural and human-made pollutants from East Asia into the SCS basin over long distances. In addition to continental outflow from East Asia, BB emissions from surrounding areas notably influence aerosol concentrations over the SCS. During the summer monsoon months, particularly August to October, persistent peatland and forest fires across the Maritime Continent (MC) generate large smoke plumes that drift toward the southern SCS (Ravindra Babu et al., 2023). Moreover, extensive open BB in spring over Peninsular Southeast Asia (PSEA), including Myanmar, Thailand, Cambodia, Laos, and Vietnam, serves as a key source of aerosols affecting the SCS atmosphere (Chan et al., 2003; Ou-Yang et al., 2012; Yadav et al., 2017; Liao et al., 2021; Wang et al., 2021; Pani et al., 2023; Wang et al., 2025; Huang et al., 2024). This region is recognized as a global hotspot for BB (Lin et al., 2013; Reid et al., 2013; Cohen, 2014; Cohen et al., 2017; Pani et al., 2019), significantly contributing to carbon emissions and aerosol loading during the peak fire season in March and April (Ravindra Babu and Lin, 2023). These fires mainly stem from annual slash-and-burn farming practices across PSEA (Lee et al., 2016; Tsay et al., 2016; Huang et al., 2020), releasing substantial particulate matter and trace gases into the air (Ou-Yang et al., 2022). As a result, aerosol variability in the SCS region is largely driven by interactions between regional emission sources and the prevailing monsoon circulation, which influence aerosol transport, dispersion, and accumulation within the basin (Pani et al., 2023).

The year 2023 saw exceptional wildfires worldwide due to record-high global mean surface temperatures, which affected carbon emissions and aerosol levels (Esper et al., 2024; Forster et al., 2024; Min, 2024; Raghuraman et al., 2024; Kolden et al., 2024; Liu et al., 2024; Byrne et al., 2024; MacCarthy et al., 2024). It has been reported that 70 % of total burning occurs in the Northern Hemisphere (Kolden et al., 2024). Among all, Canadian wildfires emerged as the primary hotspot, with significant fires in both the eastern and western regions causing notable increases in carbon monoxide (CO) and tropospheric aerosols over the past twenty years (Liu et al., 2024; Byrne et al., 2024; MacCarthy et al., 2024). Although the unprecedented Canadian wildfires in 2023 received considerable scientific attention and were well documented in several studies, the record-breaking aerosol loading over the SCS in April 2023 attracted relatively little international attention. The historic event over the SCS in April 2023 can be seen through the Moderate Resolution Imaging Spectroradiometer (MODIS) Aqua AOD anomalies compared to the long-term mean (2003–2022), which shows extreme positive anomalies over the SCS and surrounding regions during that month, contrasting with the rest of the globe (Fig. 1). However, AOD anomalies in May illustrate the absence of positive anomalies over the SCS and instead show higher positive anomalies over North America, which are related to the Canadian wildfires. The time series of monthly mean AOD over the SCS further confirms a record-high AOD in April 2023 relative to the MODIS data from 2003 to 2023 (Fig. 2d). The exceptional aerosol loading in April 2023 is unusual for remote marine locations such as the SCS and warrants further investigation. In this study, we investigated the factors and physical processes that contributed to the unprecedented aerosol levels observed in April 2023, using extensive data collected from multiple sources over an extended period. The following three major topics are examined in detail within this study:

- How extreme are these AOD anomalies, and what magnitude was increased?
- What are the sources for these record-breaking aerosol loadings over SCS?
- Were dynamic and large-scale circulations responsible for this event?

2 Data and Methodology

2.1 Data

This study relies entirely on publicly available data, covering the period from 2003 to 2023. We used data products from various satellite measurements, ground-based observations, and reanalysis products.

2.1.1 Satellite remote sensing measurements

Moderate Resolution Imaging Spectroradiometer (MODIS)

MODIS is a passive sensor aboard the Aqua and Terra satellites, which are in sun-synchronous orbits and cross the Equator in the morning (Aqua) and afternoon (Terra). From MODIS satellite measurements, we utilized aerosol optical depth (AOD), fire counts, fire radiative power (FRP), cloud fraction, and burned area products. We used Level 3 monthly AOD at $1^\circ \times 1^\circ$ spatial resolution derived from the mean of the Dark Target and Deep Blue Combined Aerosol Products from the Terra satellite (MOD08_M3 Collection 6.1)

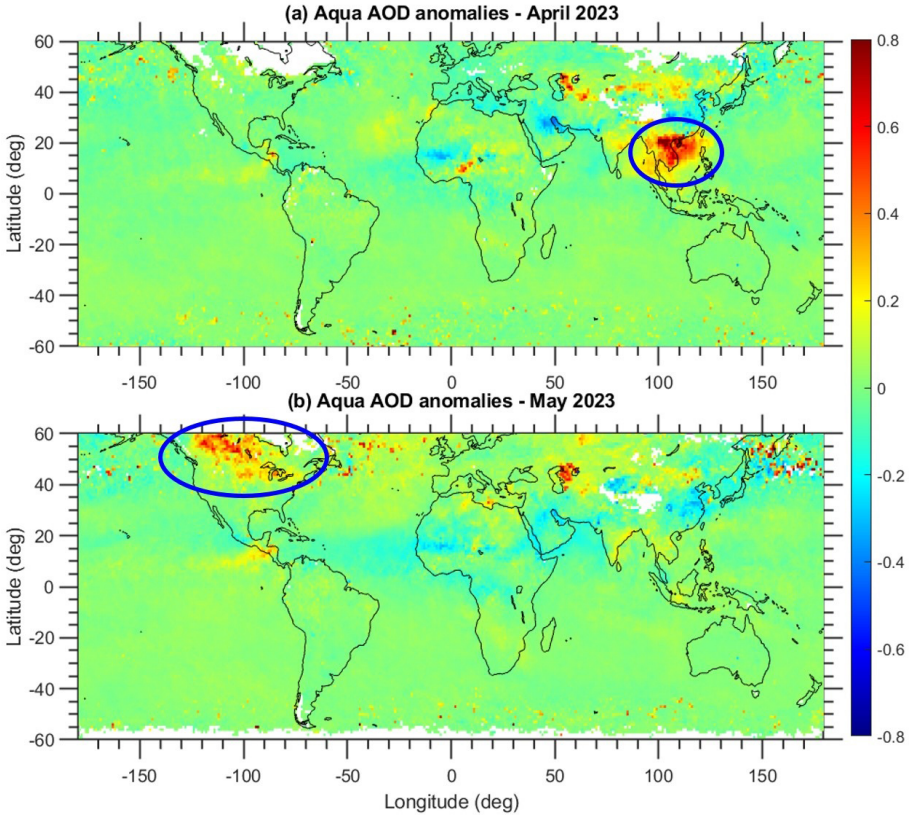

Figure 1. MODIS Aqua measured AOD anomalies in **(a)** April 2023 and **(b)** May 2023 compared to the long-term mean (2003–2022). The highlighted circles in **(a)** and **(b)** indicate the AOD anomalies over the South China Sea (SCS) and Canada regions. This figure highlights that the AOD anomalies observed by MODIS are significant and particularly pronounced over the SCS compared to the other areas globally. It illustrates the unique characteristics of April 2023 compared to long-term mean. Data visualizations produced using MATLAB R2020a (https://matlab.mathworks.com, last access: 11 June 2026).

and Aqua satellite (MYD08_M3 Collection 6.1) (Platnick et al., 2015; Buchholz et al., 2021). For MODIS AOD, the estimated uncertainty is approximately ±0.05 over ocean and ±0.15 over land. The Collection 6.1 (C6.1) products used in this study have been shown to capture temporal variations effectively and agree closely with ground-based observations (Wei et al., 2019a). Validation against AErosol RObotic NETwork (AERONET) measurements demonstrates that the merged Dark Target and Deep Blue (DTB) products accurately capture aerosol variability at both regional and global scales (Sayer et al., 2014; Wei et al., 2019b). Additionally, we used MODIS's daily fire counts and fire radiative power (FRP) products (Giglio et al., 2006, 2016, 2018). Direct fire counts from MODIS were obtained from the Fire Information for Resource Management System (FIRMS) dataset. We selected all MODIS fire counts from the Terra and Aqua sensors with a confidence level of at least 80 %. Finally, we utilized Cloud Fraction data from both the Terra and Aqua satellites.

Measurements Of Pollution In The Troposphere (MOPITT)

MOPITT is a multi-channel thermal infrared (TIR) and near-infrared (NIR) instrument operating on board the sun-synchronous polar-orbiting NASA Terra satellite. This study uses a version 9 (MOP03TM_9) gridded monthly product (Worden et al., 2010; Deeter et al., 2019). For more details on the retrieval algorithm, validation, and uncertainties in MOPITT CO, see Deeter et al. (2019).

Atmospheric Infrared Sounder (AIRS)

In addition to the MOPITT measurements, we used CO from the AIRS instrument on the NASA Aqua satellite, which provides CO at multiple vertical levels twice daily and has near-global coverage. AIRS uses wavenumbers 2183–2200 cm^{-1} (4.58–4.5 µm) for retrieving CO (McMillan et al., 2005). The V9 level 3 CO product, available at $1° \times 1°$ resolution at 700 and 500 hPa levels, was utilized in the present study. AIRS sensitivity to CO is broad and optimal in the mid-troposphere between approximately 300 and 600 hPa (Warner et al., 2007,

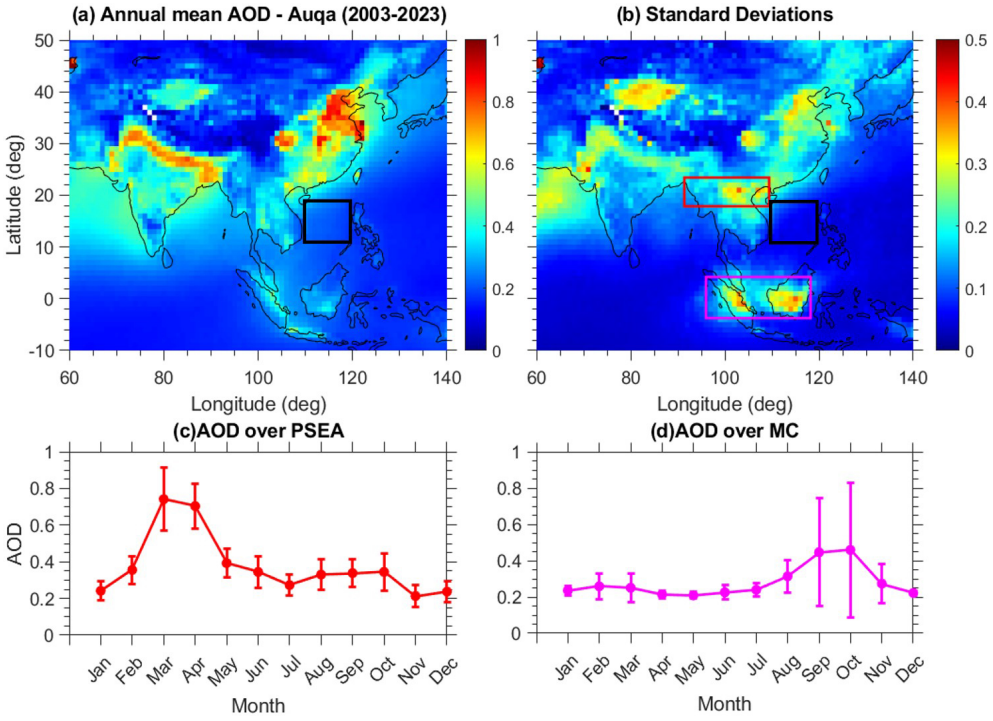

Figure 2. Climatological mean distribution of MODIS **(a)** Aerosol Optical Depth (AOD) and **(b)** respective standard deviations. The black box illustrated in both figures emphasizes the specific area of the South China Sea (SCS) that is the primary focus of this research. (11–18° N, 109–119° E). The red and magenta boxes indicate the PSEA and MC, two significant biomass-burning regions near the SCS. The long-term average seasonal variation in AOD is illustrated over **(c)** PSEA and **(d)** MC.

2013; AIRS project, 2019). CO retrievals exhibit a 6 %–10 % bias between 900 and 300 hPa with a root mean square error of 8 %–12 % (McMillan et al., 2011). In addition to CO, we also utilized, surface temperature, and outgoing longwave radiation (OLR) data from the AIRS satellite.

Global Precipitation Climatology Project (GPCP)

The Global Precipitation Climatology Project (GPCP) Version 3.2 Satellite-Gauge (SG) Combined Precipitation Data Set was used during the study period. The data is available for download from https://measures.gesdisc.eosdis.nasa.gov/data/GPCP/GPCPMON.3.2/ (last access: 5 June 2025).

Cloud-Aerosol LIDAR with Orthogonal Polarization (CALIOP)

The CALIOP sensor on the Cloud-Aerosol Lidar and Infrared Pathfinder Satellite Observations (CALIPSO) satellite provides data on atmospheric aerosols, including aerosol layer heights and thicknesses, optical depth, aerosol type, and other optical properties (Omar et al., 2009; Kim et al., 2018). In our study, we used vertical aerosol-type images available on the CALIPSO website.

2.1.2 Reanalysis/model products

MERRA-2 reanalysis

We used monthly mean geopotential height, wind vectors (zonal and meridional wind speeds), and, total column black carbon, organic carbon, and particulate matter from the Modern-Era Retrospective Analysis for Research and Applications, version 2 (MERRA-2). MERRA-2 is the latest atmospheric reanalysis data produced by the NASA Global Modeling and Assimilation Office (GMAO; Gelaro et al., 2017). The horizontal resolution of the MERRA-2 reanalysis is $0.5° \times 0.625°$.

Global Land Data Assimilation System (GLDAS)

Monthly mean soil moisture content (10–40 cm underground) from the Global Land Data Assimilation System (GLDAS)_NOAH025_M v2.1 is utilized. The data can be downloaded from https://hydro1.gesdisc.eosdis.nasa.gov/data/GLDAS/GLDAS_NOAH025_M.2.1/ (last access: 5 June 2025).

Table 1. Details of various data products used in the present study.

Data	Resolution	Source
Aerosol Optical Depth (AOD)	$1° \times 1°$	Aqua and Terra satellite/MODIS
Carbon Monoxide (CO)	$1° \times 1°$	MOPITT and AIRS
Burned Area (BA)	500 m	Aqua and Terra satellite/MODIS
MODIS Collection 6.1 Fire Anomalies		combined Terra and Aqua satellite/MODIS
Wind and Geopotential Height	$0.5° \times 0.625°$	MERRA reanalysis

2.1.3 Ground-based observations

AERONET

In this study, we use the latest version (V3) of Level 2.0 AERONET data from two stations: Dongsha Island (also called the Pratas Islands; Dongsha_Island, 20.70° N, 116.73° E, 5 m a.s.l.) and Lulin Atmospheric Background Station (LABS, 23°28′ N, 120°52′ E, 2 862 m; Sheu et al., 2010). These offer cloud-screened, quality-checked direct-sun AOD retrievals with uncertainties of about ±0.01 in the visible and ±0.02 in the ultraviolet range (Giles et al., 2019; Sinyuk et al., 2020).

The summary of the major data used in the present study is presented in Table 1.

2.2 Methodology

The anomalies in the various parameters for April 2023 were estimated by subtracting the April background long-term mea (2003–2022) from April 2023 value.

The magnitude of the AOD / CO enhancement in April 2023 above the long-term background was determined by comparing the average of April 2003–2022. We obtained the percentage change in AOD / CO relative to the respective background using Eq. (1):

$$\text{Relative change in percentage} = \left(\frac{x_{i-\overline{x}}}{\overline{x}}\right) \times 100 \quad (1)$$

where x_i represents the monthly mean of April in 2023, and $\overline{x}$ is the long-term mean of April calculated using the data from 2003 to 2022.

3 Results and Discussion

3.1 Record-breaking aerosol loading over SCS in April 2023

Aerosol optical depth (AOD) is a common metric for measuring atmospheric aerosol loading and is crucial for radiative forcing assessments (Hirsch and Koren, 2021). In this study, we use AOD data from the MODIS instruments aboard the Aqua and Terra satellites for the period. Before analyzing the unusual AOD conditions observed in April 2023, we first characterize the long-term AOD behavior over the study area using two decades of MODIS data. The spatial patterns of the long-term annual mean AOD and its associated standard deviation across the Asian region are shown in Fig. 2a and b, respectively. Additionally, the long-term monthly-mean variability of AOD over the two main BB regions surrounding the SCS, namely PSEA and the MC, is shown in Fig. 2c and d. The relatively low AOD levels and small standard deviations over the SCS suggest a predominantly clean marine environment. The seasonal cycle of AOD shows clear peaks linked to regional BB activities (Fig. 2c and d). Over PSEA, AOD peaks during March–April, while over the MC, the peak occurs in September–October. These seasonal maxima align with well-known BB activity periods in these areas (Ravindra Babu and Lin, 2023; Chang et al., 2024). The fire season over the MC usually runs from August to October, whereas PSEA experiences intense BB activity from January to April, with a notable peak in March.

To emphasize the anomalous conditions in April 2023, we present the spatial distribution of April AOD over the study region for both the long-term average and April 2023. The long-term average April AOD for 2003–2022 and the corresponding April 2023 AOD distribution are shown in Fig. 3a and b. Moreover, the time series of monthly mean AOD from 2003 to 2023 over northern PSEA (17–23° N, 99–106° E) and the SCS (11–18° N, 109–119° E) are displayed in Fig. 3c and d. The AOD distribution in April over two decades indicates high aerosol loading from northern Laos to coastal South China (15–25° N, 100–120° E). In April 2023, extreme AOD values extended from PSEA to South China and SCS, with the highest values centered between northern Laos and the SCS. Record-breaking AOD levels were observed for the area averaged over the SCS in April 2023, showing a nominal increase in northern PSEA (Fig. 3c). However, the highest AOD value for northern PSEA in April 2023 correlates with record AOD over the SCS. Long-term monthly mean AOD from Aqua and Terra (2003–2023) exhibited a strong correlation of 0.97, confirming the consistency and reliability of these observations (Fig. S1a in the Supplement). To assess the magnitude of the increase, we estimated the percentage change in AOD by comparing April 2023 with the long-term April average from 2003 to 2022.

Figures 4a and 4b illustrate the spatial extent of AOD anomalies, shown as percentage changes, based on data from

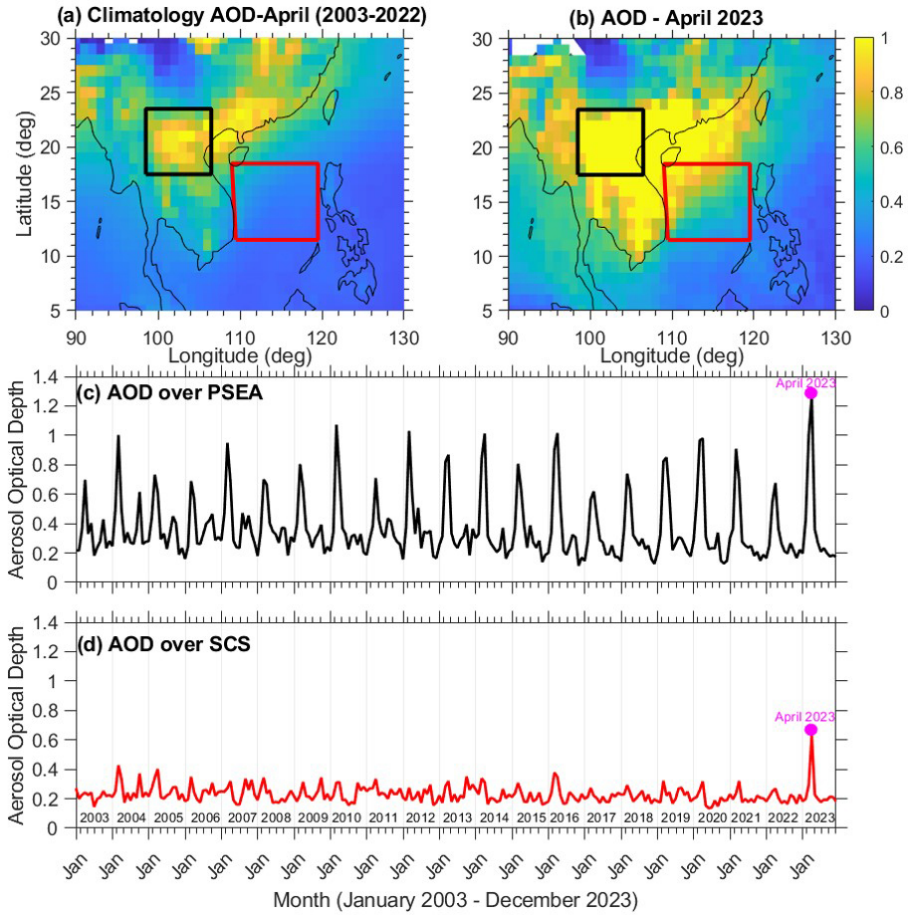

Figure 3. Spatial distribution of **(a)** Inter-annual (2003 to 2022) monthly average AOD values for April. **(b)** Monthly AOD values for April 2023. A notable increase in AOD values is observed over the Peninsular Southeast Asia (PSEA) and the South China Sea (SCS). AOD distribution averaged in April over the past two decades showed a belt of high aerosol loading extending from northern Laos to the southern coast of China. During April 2023, extreme AOD values were observed across the entire PSEA, extending to coastal South China and the SCS. **(c)** Time series of average monthly mean AOD values over the northern PSEA (17–23° N, 99–106° E), and **(d)** over the SCS (11–18° N, 109–119° E) from January 2003 to December 2023. The magenta dot in subplots **(c)** and **(d)** marks the AOD values during April 2023.

MODIS Aqua and Terra satellites. In April 2023, there was a widespread and unexpected increase of about 150 % across most of the SCS and southern Bay of Bengal (BoB), with anomalies surpassing roughly 4 standard deviations. The area-averaged AOD anomalies (%) over the SCS, indicated by the black line for Aqua and the red line for Terra, reveal that the April 2023 peak was the highest on record compared to data from 2003 to 2023, emphasizing the extreme AOD intensity that month. These satellite observations were also supported by ground-based measurements from AERONET. The only operational AERONET remote station downwind of PSEA BB, with over a decade of continuous AOD measurements (Fig. S2a in the Supplement), within the SCS region, is located on Dongsha Island (also known as Pratas Island, 20.70° N, 116.73° E; 5 m a.s.l.). Analysis of monthly mean AOD data from Dongsha Island indicates that April 2023 had the highest AOD value during the observational period from January 2009 to December 2023 (Fig. S2c in the Supplement). AERONET comparisons show strong correlations with MODIS AOD: 0.86 for Aqua and 0.87 for Terra (Fig. S3 in the Supplement), supporting the reliability of the satellite observations. Because AOD is a column-integrated measure, it does not provide information on the vertical distribution of aerosols. To address this limitation, we further analyzed vertical distribution images of aerosols from the Cloud-Aerosol Lidar and Infrared Pathfinder Satellite Observation (CALIPSO), which reveal pronounced enhancements in smoke aerosol over the SCS (Fig. 5). Elevated smoke layers were also observed over the southern BoB in April 2023, predominantly within the mid-troposphere at altitudes of approximately 2–5 km. Consistent with these CALIPSO lidar observations, MERRA-2 reanalysis data indicate substantial increases in aerosol mass concentrations in 2023, with black carbon (BC) increasing by ∼ 250 % and

organic carbon (OC) by ∼350 % (Fig. S4 in the Supplement). The most pronounced enhancements occur between 700 and 600 hPa, closely matching the altitude range identified by CALIPSO. The concurrence of satellite (MODIS and CALIPSO) and reanalysis data points to a severe pollution episode in April 2023 over and surrounding regions of the SCS, characterized by an elevated aerosol layer indicative of long-range-transported BB smoke. Notably, the SCS is a relatively clean remote marine region with limited local aerosol sources. In such environments, enhanced aerosol loading is typically associated with long-range transport of pollutants from surrounding continental regions (Pani et al., 2023). Given the potential influence of long-range transport of pollutants, we further analyzed variations in carbon monoxide (CO), a widely used tracer of BB emissions due to its relatively long atmospheric lifetime (∼ 1–2 months) and strong association with incomplete combustion (Ravindra Babu et al., 2023). We investigated CO changes across the study region using measurements from the MOPITT and AIRS satellites, which together provide more than two decades of continuous CO observations. CO data at 700 and 500 hPa from both satellites were analyzed for the period 2003–2023, with the 500 hPa level representing the altitude of maximum sensitivity for CO retrievals (Buchholz et al., 2021).

The observed CO anomalies from the two satellites are shown in Fig. 6, revealing significantly elevated CO concentrations over the SCS in April 2023, reaching up to 3σ above the 2003–2022 climatology. Although MOPITT displays more spatially concentrated anomalies than AIRS, both datasets consistently show positive CO anomalies at both pressure levels, indicating a substantial increase in mid-tropospheric CO during this period. For MOPITT CO retrievals, primary sources of uncertainty include limitations in vertical sensitivity and potential retrieval biases (Sayer et al., 2014). However, the observed enhancements ($> 3\sigma$) are supported by independent AIRS CO measurements, reinforcing the robustness of the detected anomalies. The comparison between MOPITT and AIRS CO at 500 hPa over the SCS further shows a strong positive correlation ($R \approx 0.89$; Fig. S1b in the Supplement). Furthermore, the spatial distribution of CO anomalies closely resembles that of AOD anomalies (Fig. 4). The area-averaged anomalies of AOD and 500 hPa CO over the SCS in April during 2003–2023 exhibit a strong positive correlation ($R = 0.81$; Fig. 7), suggesting that long-range transport of pollution plays an important role in modulating aerosol variability in this region. The bubble chart further highlights the exceptional severity of the April 2023 event compared with previous years (Fig. 7). Because CO is primarily produced by incomplete combustion, elevated concentrations far from major traffic or industrial sources strongly suggest BB and wildfire emissions. The strong similarity between the spatial distributions of CO and AOD anomalies suggests that the increased aerosol loading was driven by BB in April 2023. This indicates that smoke was likely transported from surrounding regions toward the SCS and the BoB, which are located near major BB hotspots, including the MC and PSEA. The MC fire season typically occurs from August to October, whereas PSEA experiences a BB season from January to April, peaking in March (Fig. 2). These seasonal characteristics strongly suggest that the elevated AOD levels observed over the SCS in April 2023 were likely linked to BB activity in PSEA PSEA (Lin et al., 2009, 2017). Overall, the April 2023 event is notable for its exceptional intensity and extensive spatial coverage. The MODIS AOD anomalies were approximately four times higher than the long-term mean across much of the SCS and the southern BoB during April 2023. Such anomalously high aerosol loading over the SCS may have important implications for the regional climate and the hydrological cycle, highlighting the need for further investigation into the underlying drivers and physical mechanisms responsible for this event.

3.2 Transport and Source Attribution of the April 2023 Aerosol Event

From the previous section, it is clear that most aerosols are free-troposphere-dominated and located primarily in the ∼ 2–5 km region over the SCS. To determine the source regions responsible for elevated aerosol concentrations over the SCS in April 2023, backward air-mass trajectories were computed using the NOAA HYSPLIT model. Trajectories were initialized at 15° N, 115° E, at 3 km a.s.l., corresponding to the altitude range (2–5 km) of the elevated aerosol layer observed in CALIPSO and MERRA-2 profiles. Daily 72 h trajectories (Fig. 8a) indicate that air masses arriving over the SCS predominantly originated from northern PSEA. When overlaid on the monthly mean MODIS AOD (Fig. 8b), these trajectories reveal transport pathways that coincide with regions of high aerosol loading, strongly suggesting that long-range transport of PSEA BB smoke likely transported to the SCS. To examine the BB activity during April 2023, MODIS fire counts and burned area (BA) data were used. The spatial distributions of MODIS fire counts and BA for April 2023 (Fig. 9a–b) show that BB activity was overwhelmingly concentrated in northern PSEA, particularly in northern Laos and adjacent regions of Myanmar and Thailand. Minimal fire activity and BA were observed over the MC and southern China; therefore, these regions were excluded from source-region calculations. Analysis of inter-annual variability in April BB activity over PSEA from 2003 to 2023 (Fig. 9c–d), considering only fire detections above the 80 % confidence level, indicates substantial year-to-year fluctuations. Notably, April 2023 recorded the highest burned area (∼ 2.27 Mha) over the 21-year period, highlighting the exceptional intensity of BB activity that month.

Country-level statistics (Table 2) further highlight the dominant contribution from Laos, which accounted for 11 877 fires (56.0 %), 1.53×106 MW of fire radiative power (FRP; 63.5 %), and 1.08×106 ha of burned area (47.7 %). Notably, the BA observed in April 2023 represents the

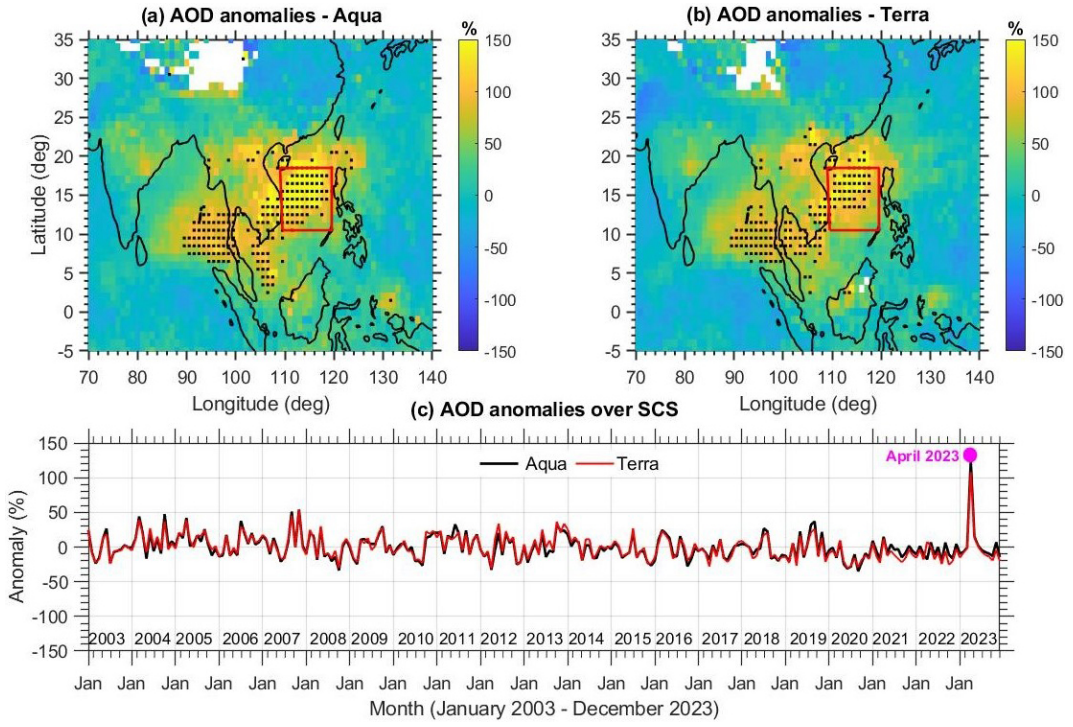

Figure 4. Spatial distribution of the change (%) in Aerosol Optical Depth (AOD) values during April 2023 compared with the inter-annual April average (2003–2022). **(a)** AOD anomalies are obtained from the MODIS Aqua and **(b)** from the MODIS Terra satellite. The black dots indicate that the anomalies exceed 4σ of the long-term mean. **(c)** Time series of area-averaged AOD anomalies expressed in percentage change over the South China Sea (SCS) domain from the Aqua (black line) and Terra (red line) satellites. The most pronounced enhancement occurred over the SCS, where April AOD anomalies exceeded 4σ above the long-term mean.

highest monthly value in the available dataset (2002–2023; Fig. S5 in the Supplement). Approximately 60 % of Laos is forested (Fig. S6 in the Supplement), with much of this forest located in northern Laos where the majority of fires occurred during April 2023 (Fig. 9a). Myanmar contributed the second-largest share, with 7 054 fires (33.3 %), 7.78×105 MW of FRP (32.3 %), and 9.15×105 ha of burned area (40.3 %). Thailand, Vietnam, and Cambodia contributed comparatively smaller burned areas of 1.21×105 ha, 1.30×105 ha, and 2.20×104 ha, respectively. In total, 21 198 fires across PSEA produced approximately 2.41×106 MW of FRP in April 2023. These results strongly suggest that intense BB activity over northern PSEA, likely contributed substantially to the exceptional aerosol loading observed over the SCS in April 2023. However, two key questions remain: (i) what factors triggered the anomalously strong fire activity in Laos during April 2023, and (ii) why were BB aerosols transported unusually far southward across the SCS and into the southern BoB, rather than following the more typical transport pathways toward Taiwan and the north western Pacific? To address these questions, we next examine the large-scale meteorological and dynamical circulation conditions prevailing during April 2023.

3.3 Large-scale meteorological and dynamical circulation anomalies in April 2023

In this section, we examine the meteorological and large-scale dynamical circulation anomalies associated with the April 2023 event. Figure 10 presents the spatial distribution of anomalies in key meteorological parameters during April 2023 relative to the 2003–2022 climatological mean. As shown in Fig. 10, Outgoing Longwave Radiation (OLR) anomalies indicate suppressed convective activity over PSEA during April 2023. Reduced convection was accompanied by negative precipitation anomalies, elevated surface temperatures, and pronounced soil moisture (SM) deficits. These conditions are spatially consistent with the regions of enhanced fire counts and BA observed by MODIS over northern Laos (Fig. 9). Long-term SM anomalies over northern Laos reached exceptionally low values in April 2023, representing the lowest levels in the past two decades (Fig. S7a–b in the Supplement). To further examine the persistence of these conditions, we analyzed the temporal evolution of SM anomalies during 2021–2023. The results show maximum positive anomalies in March 2022 and a transition to strong negative anomalies by April 2023, indicating a prolonged drought from winter 2022 to April 2023 (Fig. S7c in the Supplement). We further assessed the relationship be-

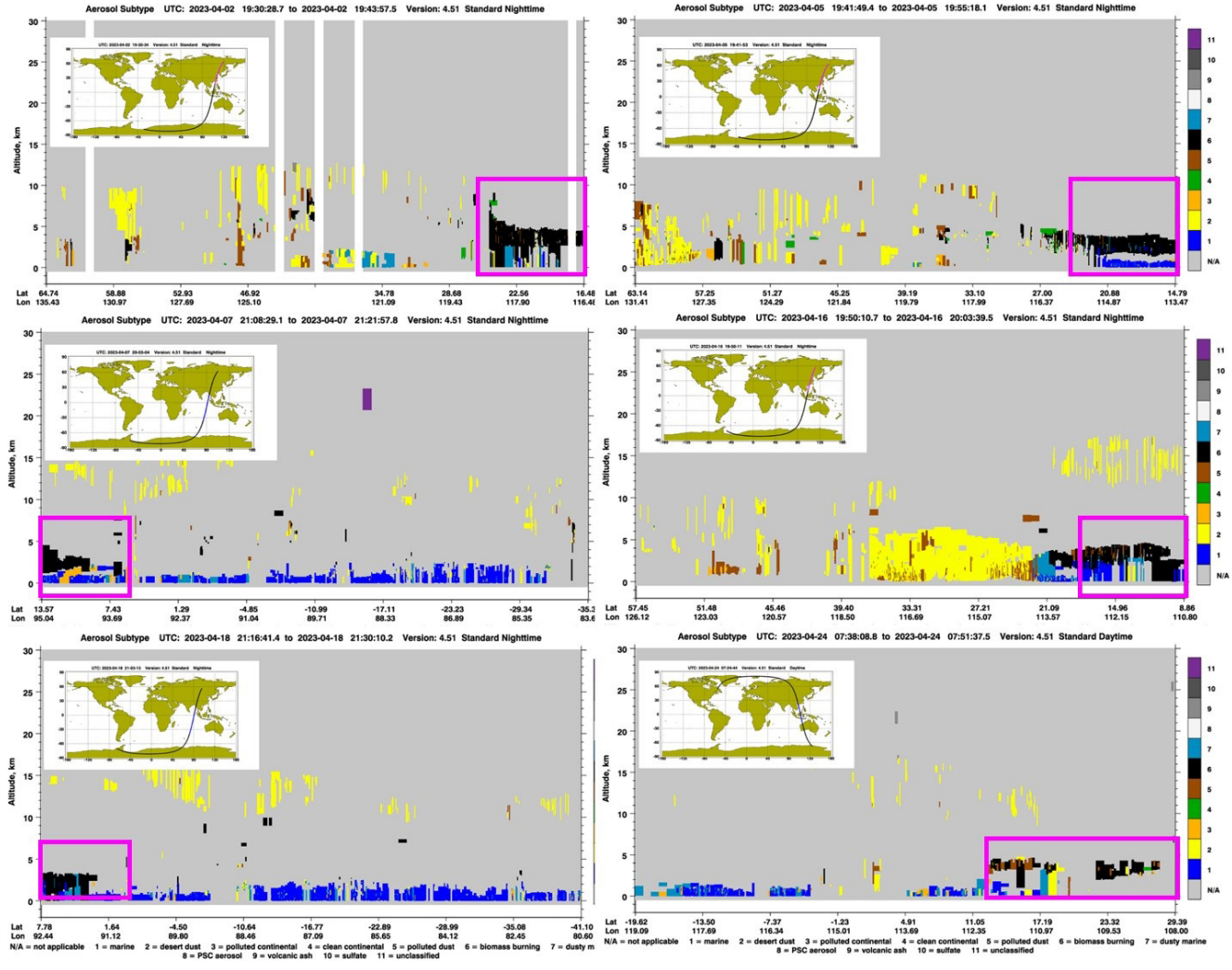

Figure 5. Aerosol subtype images obtained by the CALIPSO observations during various days in April 2023. The highlighted magenta box indicates elevated smoke over the South China Sea (SCS) and the southern Bay of Bengal. Smoke aerosol is shown in black.

Table 2. MODIS total fire counts, the corresponding total accumulated fire radiative power (FRP), and the burned area (BA) observed over peninsular Southeast Asia (PSEA) and each country within PSEA in April 2023. The percentage contribution of each country to the total number of fires, the total FRP, and the BA of PSEA is shown in brackets.

Country	Total Fires	Fire Radiative Power (MW)	Burned Area (ha)
PSEA	21 198	2 407 283	2 272 099.89
Country	Total Fires	FRP	BA
Cambodia	242 (1.14 %)	13 402 (0.5 %)	21 959.5 (0.97 %)
Laos	11 877 (56.02 %)	1 530 000 (63.5 %)	1 084 050 (47.71 %)
Myanmar	7054 (33.27 %)	777 970 (32.32 %)	915 175.7 (40.27 %)
Thailand	1322 (6.24 %)	50 276 (2.1 %)	120 573.7 (5.31 %)
Vietnam	703 (3.32 %)	35 634 (1.5 %)	130 340.7 (5.74 %)

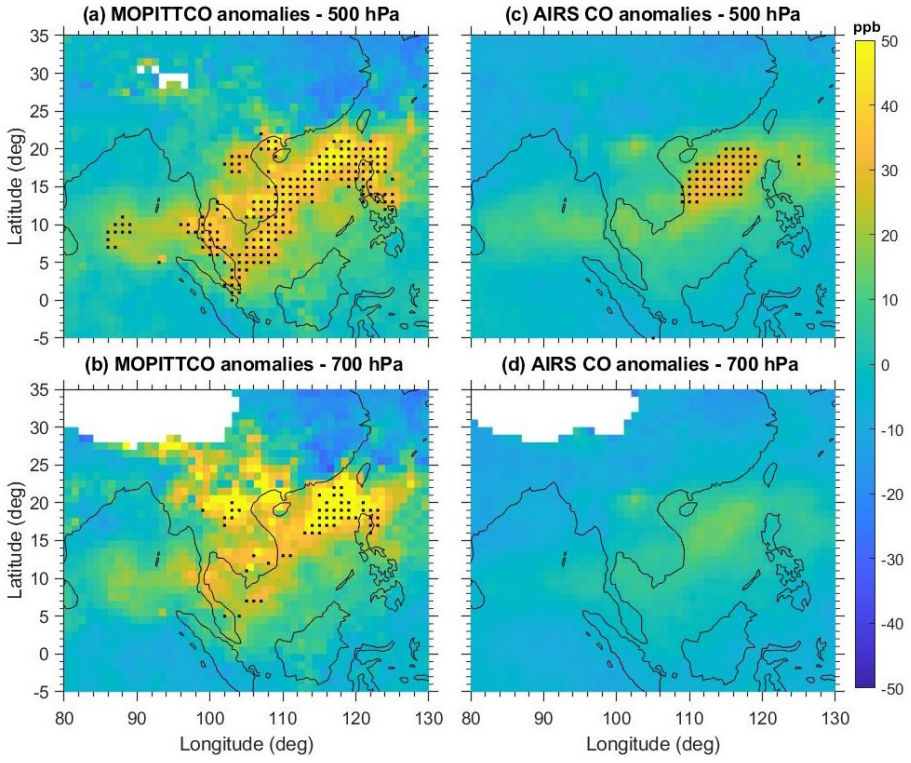

Figure 6. Spatial distribution of carbon monoxide (CO) anomalies in April 2023 at **(a)** 500 hPa and **(b)** 700 hPa from MOPITT satellite measurements. Panels **(c)** and **(d)** show the corresponding CO anomalies at 500 and 700 hPa derived from AIRS satellite observations. Anomalies are calculated relative to the long-term April mean for 2003–2022. Black dots indicate regions where anomalies exceed the 3σ significance threshold.

tween SM anomalies and fire activity over Laos. Standardized fire anomalies and SM anomalies (Fig. S8 in the Supplement) reveal a significant inverse relationship: reduced SM is associated with enhanced fire activity. In April 2023, extreme negative SM anomalies coincided with strong positive fire anomalies, highlighting the role of severe surface drying in promoting intense BB activity. A similar co-occurrence of anomalously low SM and elevated fire activity is also evident in 2016, a year previously identified as having intensified regional burning. These findings provide additional observational evidence that SM deficits are linked to enhanced fire activity over PSEA. Previous studies have shown that negative SM anomalies can promote positive geopotential height anomalies in the upper troposphere, which tend to reinforce local high-pressure conditions and enhance surface warming (e.g., Fischer et al., 2007; Dong et al., 2023). Motivated by this mechanism, we next examine the large-scale dynamical circulation patterns during April 2023 to understand how atmospheric dynamics may have contributed to the observed meteorological anomalies and the anomalous transport of BB aerosols.

Our analysis focuses on geopotential height and horizontal wind fields at the 700 and 500 hPa levels. The geopotential height fields (Z700 and Z500) in April 2023 show clear departures from the April climatology (1991–2020) (Figs. S9–10 in the Supplement). At 700 hPa, the climatological high-pressure system over the Indian region extended eastward toward PSEA, while at 500 hPa, the western Pacific subtropical anticyclone shifted westward to lie directly over PSEA. Geopotential height anomalies relative to the 1991–2020 mean (Fig. 11a–b) reveal a pronounced anti-cyclonic circulation (positive anomalies) centered over northern PSEA ($\sim 20^\circ$ N, 100° E) at 500 hPa. Similar anticyclonic anomalies are also evident in the Z700 field over the BoB. At the same time, significant cyclonic anomalies (negative geopotential height anomalies) are observed over the Arabian Sea and the WNP at both levels. These geopotential height anomaly patterns are broadly consistent with the observed sea surface temperature (SST) anomaly distribution. Positive SST anomalies are evident over the Arabian Sea, whereas negative SST anomalies occur over the BoB (Fig. 11). Positive SST anomalies are also observed over the WNP warm pool region, where negative geopotential height anomalies are present. Collectively, these patterns suggest a low–high–low (L–H–L)-like wave train extending from the Arabian Sea to the WNP warm pool region. These findings are consistent with those of Liu et al. (2026), who proposed that enhanced convection over the

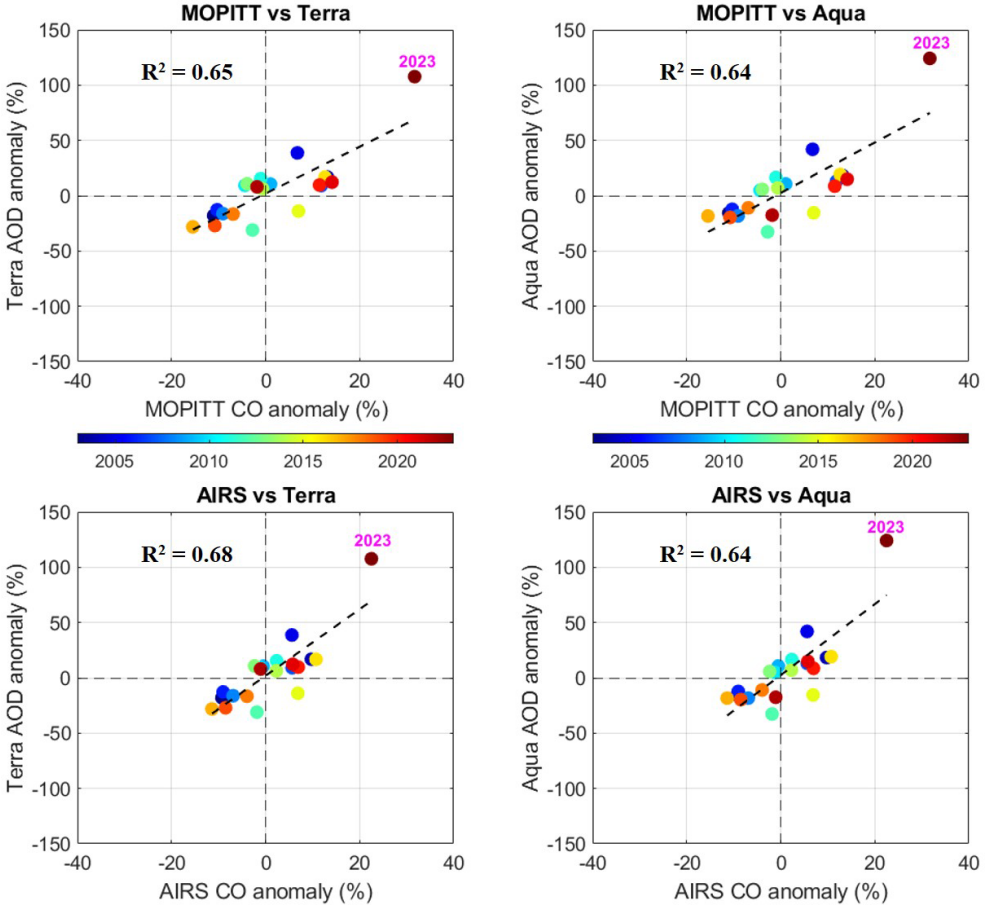

Figure 7. Bubble plot of the AOD and CO anomalies (April) over the South China Sea (SCS) during 2003–2023. Top panels for MOPITT and MODIS (Terra and Aqua), whereas the bottom panels are for AIRS and MODIS observations. The average coefficient of determination (R^2) is ∼0.65, corresponding to a correlation coefficient (R) of 0.81, indicating a statistically robust association between CO and AOD over the SCS.

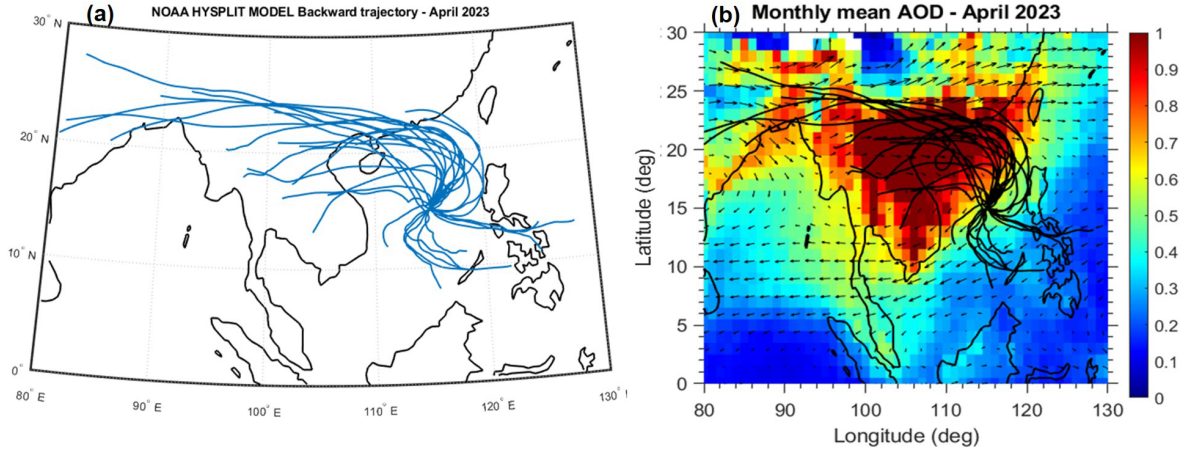

Figure 8. **(a)** Daily 72 h NOAA HYSPLIT backward trajectories ending at 12:00 UTC at a representative location (15° N, 115° E) over the South China Sea (SCS) at 3 km altitude for April 2023. **(b)** Same as **(a)**, but overlaid on the monthly mean MODIS aerosol optical depth (AOD) for April 2023.

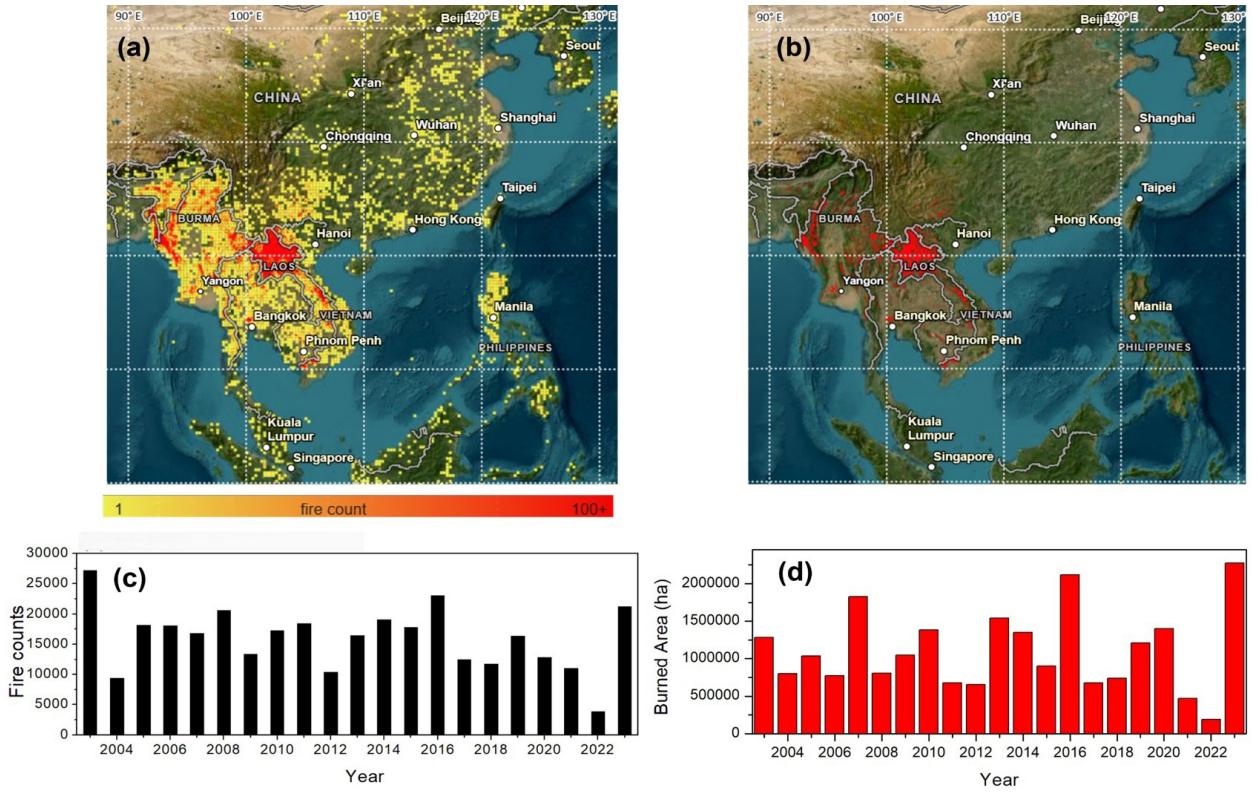

Figure 9. Spatial distribution of the **(a)** MODIS fire counts, **(b)** MODIS Global Burned Area Product in April 2023. Inter-annual variability in **(c)** Fire counts, and **(d)** Burned Area over Peninsula Southeast Asia in April from 2003 to 2023. (Source: https://firms.modaps.eosdis.nasa.gov/, last access: 11 June 2026). For inter-annual variability in fire counts, we considered those above the 80 % confidence level.

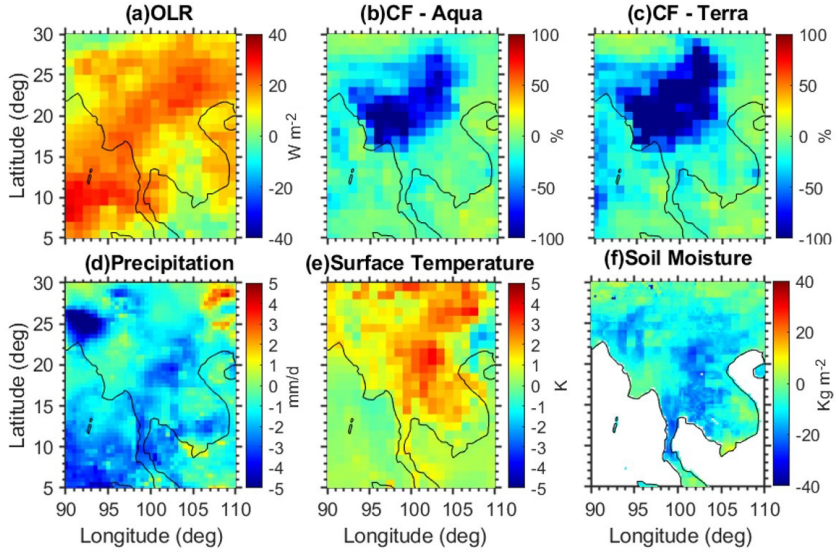

Figure 10. Surface and atmosphere conditions in April 2023. April anomalies in 2023 compared to the 2003–2022 climatological period for **(a)** Outgoing Longwave radiation (OLR), **(b)** cloud fraction (CF) from Aqua, **(c)** cloud fraction from Terra, **(d)** precipitation, **(e)** Surface Temperature, **(f)** soil moisture (10–40 cm underground). OLR and surface temperatures are obtained from AIRS satellite measurements. CF data from MODIS Aqua and Terra. Soil moisture is obtained from the GLDAS Noah Land Surface Model L4 monthly 0.25 × 0.25 degree V2.1. Precipitation data is obtained from the Global Precipitation Climatology Project (GPCP) Version 3.2.

Horn of Africa and Arabian Peninsula (HAAP) generated downstream Rossby wave propagation across South Asia and mainland Southeast Asia, contributing to anomalous upper-level cyclonic circulation over South Asia and anti-cyclonic circulation over the Indochina Peninsula (ICP) and southern China. However, their analysis was primarily based on upper-tropospheric (∼ 300 hPa) circulation fields. Although our analysis focuses on mid-tropospheric circulation anomalies at 700 and 500 hPa, the observed patterns are broadly consistent with a vertically coherent large-scale circulation response during spring 2023. These circulation anomalies, particularly mid-tropospheric anti-cyclone that suppressed convection over PSEA, are consistent with positive OLR anomalies and reduced precipitation (Fig. 10). Subsidence associated with the anti-cyclonic circulation promoted clear-sky conditions (Fig. 10) and surface warming, which, together with severe soil moisture deficits, created favorable conditions for intense BB across northern Laos. Liu et al. (2026) further showed that upper-tropospheric convergence and dynamical subsidence associated with this wave pattern contributed to persistent heat and drying over the ICP during spring 2023, potentially supporting the lower- and mid-tropospheric anti-cyclonic anomalies identified here. The circulation pattern also altered regional transport pathways. The combined influence of the WNP cyclone, the BoB anticyclone at 700 hPa, and the PSEA anticyclone at 500 hPa modified the background flow over Southeast Asia. Meridional wind anomalies (Fig. S11b–c in the Supplement) show persistent northerly flow over the SCS, enabling southward transport of smoke from northern PSEA toward the SCS and into the southern BoB. Zonal wind anomalies further indicate weakened mid-latitude westerlies and locally reversed easterlies near Japan and Taiwan associated with a strong anti-cyclonic anomaly (Fig. S11a–b in the Supplement), suppressing the typical eastward transport of smoke. Consistent with this, AOD observations from the high-altitude mountain background station, namely "Lulin Atmospheric Background Station (LABS)" obtained through AERONET show no notable enhancement in April 2023 (Fig. S12 in the Supplement), indicating reduced smoke transport toward the northwestern Pacific. AERONET comparisons show strong correlations with MODIS AOD: 0.83 for Aqua and 0.84 for Terra (Fig. S13 in the Supplement), further supporting the reliability of the satellite observations as shown in the Dongsha data. Overall, the anomalous circulation pattern, characterized by a BoB anticyclone and a WNP cyclone, redirected BB plumes from northern PSEA toward the SCS and southern BoB, producing the exceptional aerosol loading observed in April 2023.

A key question is whether April 2023 was an exceptional BB year relative to PSEA, or whether similar conditions have occurred in other high-BB years. High-BB years were identified using standardized fire anomalies derived from April MODIS fire counts following the method of Vadrevu et al. (2019). For this analysis, April fire counts from 2003–2023

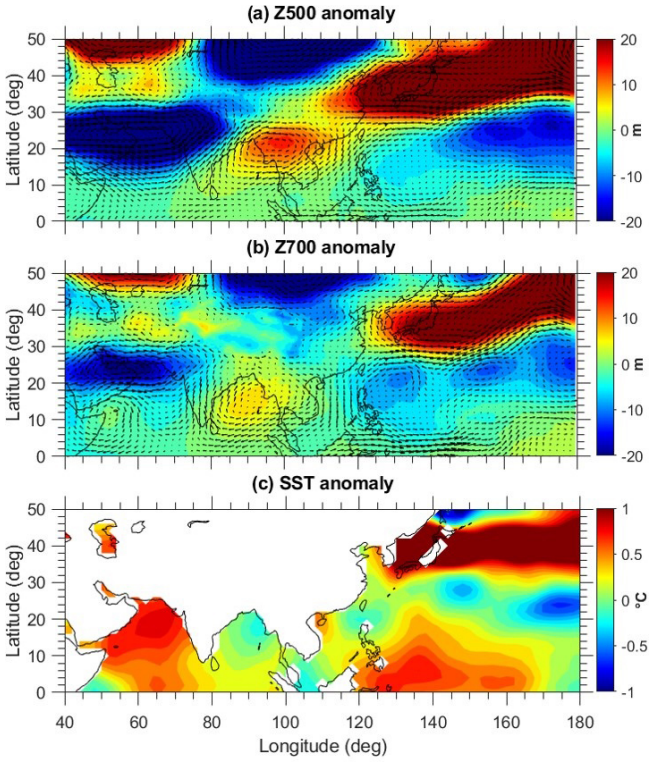

Figure 11. Spatial distribution of **(a)** 500 hPa geopotential height (Z500), **(b)** 700 hPa geopotential height (Z700), and **(c)** Sea Surface Temperature (SST) anomalies in April 2023. The anomalies are calculated by subtracting the April 2023 monthly mean from the April climatology for the period 1991 to 2020. The wind anomalies for the respective pressure levels are overlaid in Z500 and Z700 anomalies. The geopotential height and wind data are from the MERRA-2 reanalysis, while SST data are from the NOAA Extended Reconstructed SST V5.

were standardized relative to the 2003–2022 climatology over northern PSEA (17–23° N). Years with anomaly values exceeding 0.5 were classified as high-BB years (Fig. S14), including 2003, 2006, 2008, 2010, 2014, 2015, 2016, and 2023. Composite analyses of MODIS AOD, 500 hPa geopotential height (Z500), and wind vectors were conducted to characterize typical aerosol and circulation patterns during high-BB conditions. Figure 12a–c presents the spatial distributions of composite AOD for high-BB years, AOD during April 2023, and their anomalies, respectively, while Fig. 12d–f shows the corresponding Z500 and wind vector fields. Relative to the high-BB composite, April 2023 exhibited substantially higher AOD across PSEA, the SCS, and the southern BoB, indicating enhanced regional aerosol loading. The Z500 field further showed pronounced positive anomalies over northern PSEA, reflecting a stronger, more spatially coherent anti-cyclonic circulation than under typical high-BB conditions. Correspondingly, wind anomalies revealed enhanced northerly flow over the SCS during 2023, suggesting strengthened meridional aerosol transport. An additional

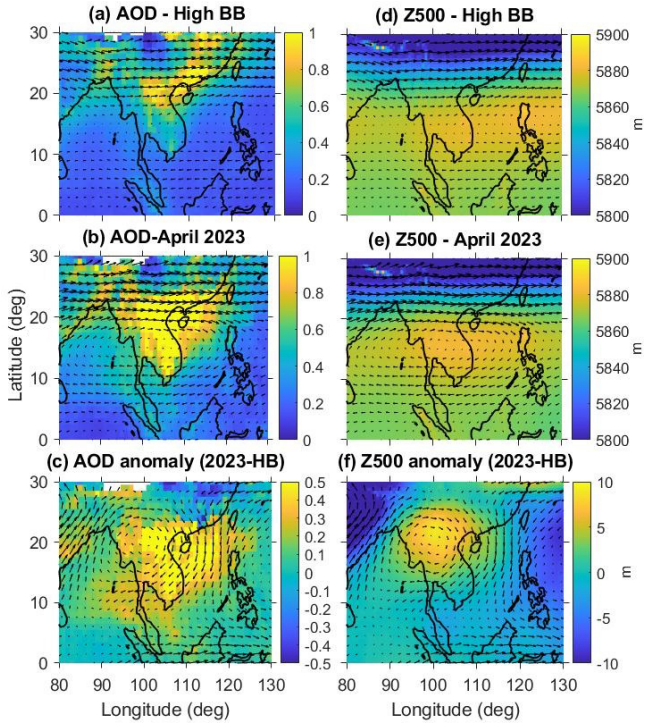

Figure 12. Spatial distribution of MODIS aerosol optical depth (AOD), MERRA-2 500 hPa geopotential height (Z500), and wind vectors during April. **(a)** Composite AOD for high biomass-burning (BB) years, **(b)** AOD in 2023, and **(c)** AOD anomalies between 2023 and the composite high-BB years. Panels **(d)**–**(f)** show the corresponding composites for Z500 and associated wind vectors for **(d)** high-BB years, **(e)** 2023, and **(f)** anomalies between 2023 and the high-BB composite, respectively.

comparison between April 2016 and April 2023 (Fig. S15 in the supplement) showed similar spatial patterns, including enhanced AOD over southern PSEA. However, the magnitude and spatial extent of the AOD enhancement were greater in 2023. The AOD anomaly between 2023 and 2016 further revealed pronounced increases over the SCS and southern BoB, coinciding with enhanced northerly anomalies. Overall, these results suggest that anomalous circulation conditions in 2023 likely amplified aerosol transport and accumulation beyond those typically associated with high-BB years.

Another question is whether inter-annual variability associated with climate oscillations, such as the El Niño–Southern Oscillation (ENSO), influenced BB activity and circulation in 2023. SST anomalies associated with ENSO strongly modulate Indo-Pacific circulation and hydroclimate, with El Niño events typically enhancing springtime fires through drought, reduced precipitation, and suppressed moisture transport (Yin, 2020; Zhu et al., 2021; Zheng et al., 2023). We constructed composites of MODIS AOD and 500 hPa wind vectors for El Niño–ensuing and La Niña–ensuing Aprils during 2003–2022 (Fig. S16 in the Supplement). The results reveal higher AOD over northern PSEA and coastal South China during El Niño-ensuing Aprils, accompanied by a stronger anti-cyclonic system over PSEA extending from the BoB, consistent with enhanced aerosol accumulation. In contrast, Aprils following La Niña show weaker circulation and lower AOD. April 2023 occurred during the transition from a triple-dip La Niña to a developing El Niño, deviating from typical ENSO-fire patterns. This unusually large-scale background is consistent with Liu et al. (2026), who noted that the extreme spring 2023 heat event over the ICP differed fundamentally from canonical ENSO-linked events, as severe regional warming and subsidence developed despite antecedent La Niña conditions.

Overall, systematic analysis of MODIS fire counts, burned area (BA), HYSPLIT back trajectories, and MERRA-2 large-scale circulation fields, we conclude that the extreme aerosol event in April 2023 was shaped not only by BB activity but also by anomalous large-scale circulation patterns. These findings highlight the combined influence of BB emissions and background meteorological conditions in producing the exceptional smoke event.

4 Summary and Conclusions

In April 2023, record-breaking aerosol loading was observed over the South China Sea (SCS). By integrating multiple satellite measurements (MODIS, MOPITT, AIRS, and CALIPSO), the MERRA-2 reanalysis, and NOAA HYSPLIT back-trajectory analysis, we systematically investigated the sources, transport pathways, and large-scale dynamical conditions associated with this extreme event. MODIS observations indicate an approximately 150 % increase in aerosol optical depth (AOD), relative to the long-term mean (2003–2022). This enhancement was accompanied by pronounced increases in carbon monoxide (CO) in the mid- to lower troposphere (700–500 hPa) as observed by MOPITT and AIRS, consistent with long-range transport of combustion-related pollution. The simultaneous increases in AOD and CO over the remote ocean support the influence of transported biomass-burning (BB) emissions from surrounding source regions. Analysis of MODIS fire counts and burned area revealed a significant enhancement in BB activity over northern PSEA and negligible BB activity over South China and the Maritime Continent. Furthermore, NOAA HYSPLIT back trajectories indicate that most air masses over the SCS originate from the northern PSEA. Together, fire counts, BA, and HYSPLIT trajectory analysis suggest that enhanced BB activity over northern PSEA likely contributed to the exceptional aerosol loading over the SCS in April 2023. Meteorological conditions characterized by suppressed convection, reduced precipitation, elevated surface temperatures, and decreased soil moisture likely promoted increased BB activity. These conditions were associated with a pronounced high-pressure (anti-cyclonic) anomaly over PSEA, as indicated by positive geopotential height anomalies at 500 hPa (Fig. 11a).

Large-scale circulation analyses further reveal a free-tropospheric pattern featuring an eastward-shifted Bay of Bengal (BoB) anticyclone and a western North Pacific (WNP) cyclone (Fig. 11b). These circulation features significantly modified regional flow over the SCS by reversing the prevailing meridional winds from southerly to northerly anomalies. In addition, the coexistence of a subtropical anticyclone over the northwestern Pacific and the WNP anomaly generated easterly wind anomalies around Taiwan. Together, these anomalous circulation patterns altered BB smoke transport pathways and facilitated aerosol accumulation over the SCS in April 2023. A schematic summary of the physical mechanisms is provided in Fig. 13.

While this study focuses on the sources, transport pathways, and dynamical drivers of the record aerosol event, its broader impacts remain to be quantified. In particular, aerosol–radiation interactions associated with elevated AOD may significantly affect regional radiative forcing, atmospheric heating profiles, and the hydrological cycle. Future work will quantify the radiative impacts of these extreme aerosol concentrations and assess their implications for regional climate. Additionally, elevated BB emissions of CO and other precursors may enhance tropospheric ozone formation, a topic that warrants further investigation. Notably, mainland Southeast Asia experienced an extreme heatwave in April 2023, with record-high temperatures (Zachariah et al., 2023; Lyu et al., 2024). While previous studies attribute this event to anthropogenic climate change, strengthened high-pressure systems, and land–atmosphere coupling, our results suggest that BB aerosols and associated greenhouse gas emissions may also have contributed to the regional heat anomaly. Key outstanding questions include how BB-derived greenhouse gases influence regional radiative trapping and how elevated aerosol concentrations modify surface radiation, cloud processes, and precipitation. Addressing these questions is essential for understanding compound climate extremes in PSEA and surrounding regions. In conclusion, this study highlights the combined role of BB emissions and large-scale dynamical conditions in shaping smoke transport over Southeast Asia, providing deeper insights into the mechanisms governing extreme regional aerosol events.

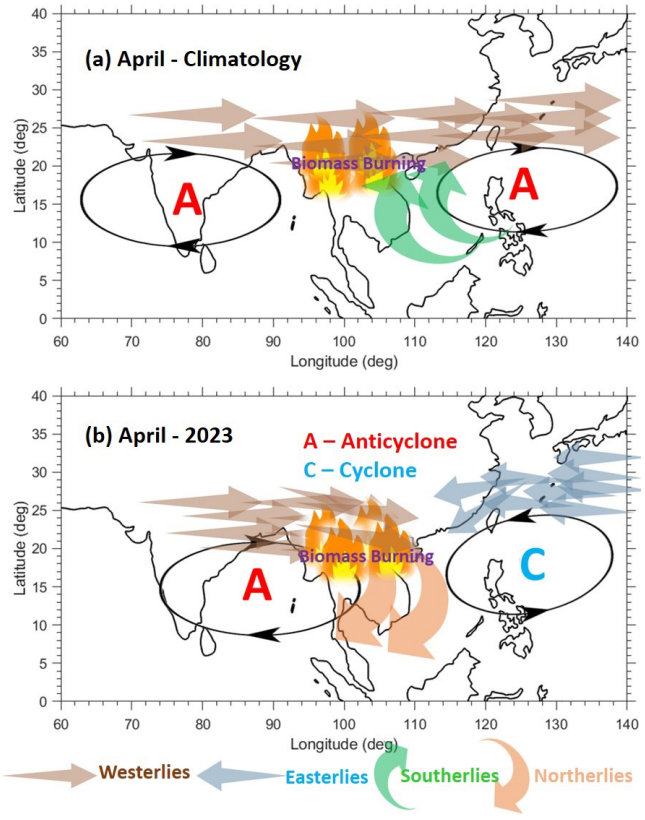

Figure 13. Schematic diagram illustrating the physical mechanisms responsible for the record-breaking aerosol loading over the South China Sea (SCS) in April 2023. The diagram summarizes the anomalous circulation and transport pathways governing biomass-burning (BB) smoke distribution. Here, "A" denotes an anticyclone anomaly and "C" denotes a cyclone anomaly. Horizontal arrows represent subtropical free-tropospheric westerlies and easterlies, while green and brown arrows indicate southerly and northerly winds, respectively. **(a)** The climatological conditions in April (1991–2020), characterized by the Bay of Bengal (BoB) and western Pacific anticyclones, as well as prevailing southwesterly and southerly winds over the SCS that favor typical smoke transport toward Taiwan and the western North Pacific (WNP). **(b)** April 2023 conditions, featuring a WNP cyclone, and an eastward-shifted BoB anticyclone. These anomalies generated persistent northerly winds over the SCS and redirected BB plumes toward the SCS and the southern BoB. Strengthened easterlies around Taiwan further inhibited eastward transport, resulting in exceptional aerosol accumulation over the SCS in April 2023.

Code and data availability. This study exclusively utilized publicly available datasets, and no new observational data were generated. All data required to evaluate the conclusions of this study are included in the paper and/or the Supplementary Information. Most figures presented in this study were generated using MATLAB R2020a. All datasets used in the study are freely available for download from their respective websites. MODIS data available from https://modis.gsfc.nasa.gov/data/dataprod/mod08.php (last access: 11 June 2026, NASA, 2026a). The AIRS and MOPITT CO data can be downloaded from https://acdisc.gesdisc.eosdis.nasa.gov/data/Aqua_AIRS_Level3/AIRS3STM.7.0/ (last access: 11 June 2026, AIRS project, 2019) and https://asdc.larc.nasa.gov/project/MOPITT/MOP02J_8 (last access: 11 June 2026, NASA, 2026b). MERRA-2 data are available online through the NASA Goddard Earth Sciences Data Information Services Center (GES DISC; https://gmao.gsfc.nasa.gov/gmao-products/merra-2/data-access_merra-2/, last access: 11 June 2026, NASA, 2026c). The MODIS fire and burned area products can be downloaded from https://firms.modaps.eosdis.nasa.gov/active_fire/(NASA, 2026d) (last access: 11 June 2026). Daily CALIPSO vertical distribution images of various aerosol types were obtained from https://www-calipso.larc.nasa.gov/products (last access: 11

June 2026, NASA, 2026e). The NOAA HYSPLIT back trajectories are retrieved from https://www.ready.noaa.gov/HYSPLIT.php (last access: 11 June 2026, Stein et al., 2015).

Supplement. The supplement related to this article is available online at https://doi.org/10.5194/acp-26-8961-2026-supplement.

Author contributions. SRB: Conceptualization, Data curation, Formal analysis, Investigation, Software, Validation, Visualization, Writing – original draft preparation, Writing – review and editing; N-HL: Conceptualization, Investigation, Funding Acquisition, Supervision, Resources, Writing – review and editing.

Competing interests. The contact author has declared that neither of the authors has any competing interests.

Disclaimer. Publisher's note: Copernicus Publications remains neutral with regard to jurisdictional claims made in the text, published maps, institutional affiliations, or any other geographical representation in this paper. The authors bear the ultimate responsibility for providing appropriate place names. Views expressed in the text are those of the authors and do not necessarily reflect the views of the publisher.

Acknowledgements. We acknowledge the National Science and Technology Council (NSTC) of Taiwan for supporting the research (grant no. 114-2111-M-008-030 and 114-2811-M-008-022). The authors thank NASA and NOAA for providing MOPITT, MODIS, CALIPSO and AIRS satellite data. We thank NASA's Global Monitoring and Assimilation Office (GMAO) for providing the Modern-Era Retrospective analysis for Research and Applications, Version 2 (MERRA-2) data.

Review statement. This paper was edited by Jason Cohen and reviewed by three anonymous referees.

References

AIRS Project: Aqua/AIRS L3 Monthly Standard Physical Retrieval (AIRS-only) 1 degree x 1 degree V7.0, NASA Goddard Earth Sciences Data and Information Services Center [data set], https://doi.org/10.5067/UBENJB9D3T2H, 2019.

Anderson, T. L., Charlson, R. J., Schwartz, S. E., Knutti, R., Boucher, O., Rodhe, H., and Heintzenberg, J.: Climate forcing by aerosol – a hazy picture, Science, 300, 1103–1104, https://doi.org/10.1126/science.1084777, 2003.

Buchholz, R. R., Worden, H. M., Park, M., Francis, G., Deeter, M. N., Edwards, D. P., Emmons, L. K., Gaubert, B., Gille, J., Martinez-Alonso, S., Tang, W., Kumar, R., Drummond, J. R., Clerbaux, C., George, M., Coheur, P.-F., Hurtmans, D., Bowman, K. W., Luo, M., Payne, V. H., Worden, J. R., Chin, M., Levy, R. C., Warner, J., Wei, Z., and Kulawik, S. S.: Air pollution trends measured from Terra: CO and AOD over industrial, fire-prone, and background regions, Remote Sens. Environ., 256, 112275, https://doi.org/10.1016/j.rse.2020.112275, 2021.

Byrne, B., Liu, J., and Bowman, K. W.: Carbon emissions from the 2023 Canadian wildfires, Nature, 633, 835–839, https://doi.org/10.1038/s41586-024-07878-z, 2024.

Chan, C. Y., Chan, L. Y., Harris, J. M., Oltmans, S. J., Blake, D. R., Qin, Y., Zheng, Y. G., and Zheng, X. D.: Characteristic of biomass-burning emission sources, transport, and chemical speciation in enhanced springtime tropospheric ozone profile over Hong Kong, J. Geophys. Res., 108, 4015, https://doi.org/10.1029/2001JD001555, 2003.

Chang, J. H.-W., Wong, Y. J., Ooi, M. C.-G., Babu, S. R., Pani, S. K., and Lin, N.-H.: Biomass-burning in critical fire region over the Maritime Continent from 2012 to 2021: A review of the meteorological influence and cloud-aerosol-radiation interactions, Atmos. Environ., 320, 120324, https://doi.org/10.1016/j.atmosenv.2023.120324, 2024.

Cohen, J. B.: Quantifying the occurrence and magnitude of the Southeast Asian fire climatology, Environ. Res. Lett., 9, 114018, https://doi.org/10.1088/1748-9326/9/11/114018, 2014.

Cohen, J. B., Lecoeur, E., and Hui Loong Ng, D.: Decadal-scale relationship between measurements of aerosols, land-use change, and fire over Southeast Asia, Atmos. Chem. Phys., 17, 721–743, https://doi.org/10.5194/acp-17-721-2017, 2017.

Crutzen, P. J. and Andreae, M. O.: Biomass-burning in the Tropics: Impact on Atmospheric Chemistry and Biogeochemical Cycles, Science, 250, 1669–1678, https://doi.org/10.1126/science.250.4988.1669, 1990.

Cui, D., Wang, J., Tan, L., and Dong, Z.: Impact of atmospheric wet deposition on phytoplankton community structure in the South China Sea, Estuar. Coast. Shelf Sci., 173, 1–8, https://doi.org/10.1016/j.ecss.2016.02.011, 2016.

Deeter, M. N., Edwards, D. P., Francis, G. L., Gille, J. C., Mao, D., Martínez-Alonso, S., Worden, H. M., Ziskin, D., and Andreae, M. O.: Radiance-based retrieval bias mitigation for the MOPITT instrument: the version 8 product, Atmos. Meas. Tech., 12, 4561–4580, https://doi.org/10.5194/amt-12-4561-2019, 2019.

Dong, Z., Yang, R., Cao, J., Wang, L., and Cheng, J.: A strong high-temperature event in late-spring 2023 in Yunnan province, Southwest China: Characteristics and possible causes, Atmos. Res, 295, 107017, https://doi.org/10.1016/j.atmosres.2023.107017, 2023.

Esper, J., Torbenson, M., and Büntgen, U.: 2023 summer warmth unparalleled over the past 2,000 years, Nature, 631, 94–97, https://doi.org/10.1038/s41586-024-07512-y, 2024.

Fischer, E. M., Seneviratne, S. I., Vidale, P. L., Lüthi, D., and Schär, C.: Soil Moisture – Atmosphere Interactions during the 2003 European Summer Heat Wave, J. Climate, 20, 5081–5099, https://doi.org/10.1175/JCLI4288.1, 2007.

Forster, P., Storelvmo, T., Armour, K., Collins, W., Dufresne, J.-L., Frame, D., Lunt, D. J., Mauritsen, T., Palmer, M. D., Watanabe, M., Wild, M., and Zhang, H.: The Earth's Energy Budget, Climate Feedbacks, and Climate Sensitivity, in: Climate Change 2021: The Physical Science Basis, Contribution of Working Group I to the Sixth Assessment Report of the Intergovernmental Panel on Climate Change, edited by: Masson-Delmotte, V., Zhai, P., Pirani, A., Connors, S. L., Péan, C., Berger, S., Caud,

N., Chen, Y., Goldfarb, L., Gomis, M. I., Huang, M., Leitzell, K., Lonnoy, E., Matthews, J. B. R., Maycock, T. K., Waterfield, T., Yelekçi, O., Yu, R., and Zhou, B., Cambridge University Press, Cambridge, United Kingdom and New York, NY, USA, 923–1054, https://doi.org/10.1017/9781009157896.009, 2021.

Forster, P. M., Smith, C., Walsh, T., Lamb, W. F., Lamboll, R., Hall, B., Hauser, M., Ribes, A., Rosen, D., Gillett, N. P., Palmer, M. D., Rogelj, J., von Schuckmann, K., Trewin, B., Allen, M., Andrew, R., Betts, R. A., Borger, A., Boyer, T., Broersma, J. A., Buontempo, C., Burgess, S., Cagnazzo, C., Cheng, L., Friedlingstein, P., Gettelman, A., Gütschow, J., Ishii, M., Jenkins, S., Lan, X., Morice, C., Mühle, J., Kadow, C., Kennedy, J., Killick, R. E., Krummel, P. B., Minx, J. C., Myhre, G., Naik, V., Peters, G. P., Pirani, A., Pongratz, J., Schleussner, C.-F., Seneviratne, S. I., Szopa, S., Thorne, P., Kovilakam, M. V. M., Majamäki, E., Jalkanen, J.-P., van Marle, M., Hoesly, R. M., Rohde, R., Schumacher, D., van der Werf, G., Vose, R., Zickfeld, K., Zhang, X., Masson-Delmotte, V., and Zhai, P.: Indicators of Global Climate Change 2023: annual update of key indicators of the state of the climate system and human influence, Earth Syst. Sci. Data, 16, 2625–2658, https://doi.org/10.5194/essd-16-2625-2024, 2024.

Gelaro, R., McCarty, W., Suárez, M. J., Todling, R., Molod, A., Takacs, L., Randles, C. A., Darmenov, A., Bosilovich, M. G., Reichle, R., Wargan, K., Coy, L., Cullather, R., Draper, C., Akella, S., Buchard, V., Conaty, A., da Silva, A. M., Gu, W., Kim, G.-K., Koster, R., Lucchesi, R., Merkova, D., Nielsen, J. E., Partyka, G., Pawson, S., Putman, W., Rienecker, M., Schubert, S. D., Sienkiewicz, M., and Zhao, B.: The Modern-Era Retrospective Analysis for Research and Applications, Version 2 (MERRA-2), J. Climate, 30, 5419–5454, https://doi.org/10.1175/JCLI-D-16-0758.1, 2017.

Giglio, L., Csiszar, I., and Justice, C. O.: Global distribution and seasonality of active fires as observed with the Terra and Aqua Moderate Resolution Imaging Spectroradiometer (MODIS) sensors, J. Geophys. Res.-Biogeo., 111, https://doi.org/10.1029/2005JG000142, 2006.

Giglio, L., Schroeder, W., and Justice, C. O.: The collection 6 MODIS active fire detection algorithm and fire products, Remote Sens. Environ., 178, 31–41, https://doi.org/10.1016/j.rse.2016.02.054, 2016.

Giglio, L., Boschetti, L., Roy, D. P., Humber, M. L., and Justice, C. O.: The Collection 6 MODIS burned area mapping algorithm and product, Remote Sens. Environ., 217, 72–85, https://doi.org/10.1016/j.rse.2018.08.005, 2018.

Giles, D. M., Sinyuk, A., Sorokin, M. G., Schafer, J. S., Smirnov, A., Slutsker, I., Eck, T. F., Holben, B. N., Lewis, J. R., Campbell, J. R., Welton, E. J., Korkin, S. V., and Lyapustin, A. I.: Advancements in the Aerosol Robotic Network (AERONET) Version 3 database – automated near-real-time quality control algorithm with improved cloud screening for Sun photometer aerosol optical depth (AOD) measurements, Atmos. Meas. Tech., 12, 169–209, https://doi.org/10.5194/amt-12-169-2019, 2019.

Hirsch, E. and Koren, I.: Record-breaking aerosol levels explained by smoke injection into the stratosphere, Science, 371, 1269–1274, https://doi.org/10.1126/science.abe1415, 2021.

Huang, H.-Y., Wang, S.-H., Huang, W.-X., Lin, N.-H., Chuang, M.-T., da Silva, A. M., and Peng, C.-M.: Influence of Synoptic-Dynamic Meteorology on the Long-Range Transport of Indochina Biomass-burning Aerosols, J. Geophys. Res.-Atmos., 125, e2019JD031260, https://doi.org/10.1029/2019JD031260, 2020.

Huang, H.-Y., Wang, S.-H., Lau, W. K. M., Wang, S.-Y. S., and da Silva, A. M.: Impact of regional climate patterns on the biomass-burning emissions and transport over Peninsular Southeast Asia, 2000–2019, Atmos. Res., 297, 107067, https://doi.org/10.1016/j.atmosres.2023.107067, 2024.

IPCC: Climate Change 2021 – The Physical Science Basis: Working Group I Contribution to the Sixth Assessment Report of the Intergovernmental Panel on Climate Change, Cambridge University Press, Cambridge, https://doi.org/10.1017/9781009157896, 2023.

Kim, M.-H., Omar, A. H., Tackett, J. L., Vaughan, M. A., Winker, D. M., Trepte, C. R., Hu, Y., Liu, Z., Poole, L. R., Pitts, M. C., Kar, J., and Magill, B. E.: The CALIPSO version 4 automated aerosol classification and lidar ratio selection algorithm, Atmos. Meas. Tech., 11, 6107–6135, https://doi.org/10.5194/amt-11-6107-2018, 2018.

Kolden, C. A., Abatzoglou, J. T., Jones, M. W., and Jain, P.: Wildfires in 2023, Nat. Rev. Earth Environ., 5, 238–240, https://doi.org/10.1038/s43017-024-00544-y, 2024.

Lee, C.-T., Ram, S. S., Nguyen, D. L., Chou, C. C., Chang, S.-Y., Lin, N.-H., Chang, S.-C., Hsiao, T.-C., Sheu, G.-R., and Ou-Yang, C.-F.: Aerosol chemical profile of near-source biomass-burning smoke in Sonla, Vietnam during 7-SEAS campaigns in 2012 and 2013, Aerosol Air Qual. Res., 16, 2603–2617, 2016.

Liao, Z. H., Ling, Z. H., Gao, M., Sun, J. R., Zhao, W., Ma, P. K., Quan, J. N., and Fan, S. J.: Tropospheric Ozone Variability Over Hong Kong Based on Recent 20 years (2000–2019) Ozonesonde Observation, J. Geophys. Res.-Atmos., 126, https://doi.org/10.1029/2020jd033054, 2021.

Lin, C. C., Chen, W. N., Loftus, A. M., Lin, C. Y., Fu, Y. T., Peng, C. M., and Yen, M. C.: Influences of the long-range transport of biomass-burning pollutants on surface air quality during 7-SEAS field campaigns, Aerosol Air Qual. Res., 17, 2595–2607, https://doi.org/10.4209/aaqr.2017.08.0273, 2017.

Lin, C.-Y., Hsu, H.-m., Lee, Y. H., Kuo, C. H., Sheng, Y.-F., and Chu, D. A.: A new transport mechanism of biomass burning from Indochina as identified by modeling studies, Atmos. Chem. Phys., 9, 7901–7911, https://doi.org/10.5194/acp-9-7901-2009, 2009.

Lin, N.-H., Tsay, S.-C., Maring, H. B., Yen, M.-C., Sheu, G.-R., Wang, S.-H., Chi, K. H., Chuang, M.-T., Ou-Yang, C.-F., Fu, J. S., Reid, J. S., Lee, C.-T., Wang, L.-C., Wang, J.-L., Hsu, C. N., Sayer, A. M., Holben, B. N., Chu, Y.-C., Nguyen, X. A., Sopajaree, K., Chen, S.-J., Cheng, M.-T., Tsuang, B.-J., Tsai, C.-J., Peng, C.-M., Schnell, R. C., Conway, T., Chang, C.-T., Lin, K.-S., Tsai, Y. I., Lee, W.-J., Chang, S.-C., Liu, J.-J., Chiang, W.-L., Huang, S.-J., Lin, T.-H., and Liu, G.-R.: An overview of regional experiments on biomass-burning aerosols and related pollutants in Southeast Asia: From BASE-ASIA and the Dongsha Experiment to 7-SEAS, Atmos. Environ., 78, 1–19, https://doi.org/10.1016/j.atmosenv.2013.04.066, 2013.

Liu, B., Fang, Y., Sun, S., Liu, L., and Cheah, W.: Extreme High Temperatures in the Indochina Peninsula and Their Association With Enhanced Convection in the Horn of Africa and Arabian Peninsula During Spring 2023, Atmos. Sci. Lett., 27, e70026, https://doi.org/10.1002/asl2.70026, 2026.

Liu, Z., Deng, Z., Davis, S. J., and Ciais, P.: Global carbon emissions in 2023, Nature Reviews Earth and Environment, 1–2, https://doi.org/10.1038/s43017-024-00532-2, 2024.

Lyu, Y., Wang, J., Zhi, X., Wang, X., Zhang, H., Wen, Y., Park, E., Lee, J., Wan, X., Zhu, S., Dung, D. T.: The characterization, mechanism, predictability, and impacts of the unprecedented 2023 Southeast Asia heatwave, npj Clim. Atmos. Sci., 7, 246, https://doi.org/10.1038/s41612-024-00797-w, 2024.

MacCarthy, J., Tyukavina, A., Weisse, M. J., Harris, N., and Glen, E.: Extreme wildfires in Canada and their contribution to global loss in tree cover and carbon emissions in 2023, Glob. Change Biol., 30, e17392, https://doi.org/10.1111/gcb.17392, 2024.

McMillan, W. W., Barnet, C., Strow, L., Chahine, M. T., McCourt, M. L., Warner, J. X., Novelli, P. C., Korontzi, S., Maddy, E. S., and Datta, S.: Daily global maps of carbon monoxide from NASA's Atmospheric Infrared Sounder, Geophys. Res. Lett., 32, L11801, https://doi.org/10.1029/2004GL021821, 2005.

McMillan, W. W., Evans, K. D., Barnet, C. D., Maddy, E. S., Sachse, G. W., and Diskin, G. S.: Validating the AIRS Version 5 CO retrieval with DACOM in situ measurements during INTEX-A and -B, IEEE T. Geosci. Remote, 49, 2802–2813, https://doi.org/10.1109/TGRS.2011.2106505, 2011.

Min, S. K.: Human influence can explain the widespread exceptional warmth in 2023, Commun. Earth Environ., 5, 215, https://doi.org/10.1038/s43247-024-01391-x, 2024.

NASA: Moderate Resolution Imaging Spectroradiometer (MODIS), NASA [data set], https://modis.gsfc.nasa.gov/data/dataprod/mod08.php (last access: 11 June 2026), 2026a.

NASA: Measurements Of Pollution In The Troposphere, NASA [data set], https://asdc.larc.nasa.gov/project/MOPITT (last access: 11 June 2026), 2026b.

NASA: Modern-Era Retrospective Analysis for Research and Applications, version 2, NASA [data set], https://gmao.gsfc.nasa.gov/gmao-products/merra-2/data-access_merra-2/ (last access: 11 June 2026), 2026c.

NASA: The Fire Information for Resource Management System (FIRMS), NASA [data set], https://firms.modaps.eosdis.nasa.gov/ (last access: 11 June 2026), 2026d.

NASA: Cloud-Aerosol Lidar and Infrared Pathfinder Satellite Observations (CALIPSO), NASA [data set], https://www-calipso.larc.nasa.gov/products (last access: 11 June 2026), 2026e.

Omar, A. H., Winker, D. M., Vaughan, M. A., Hu, Y., Trepte, C. R., Ferrare, R. A., Lee, K.-P., Hostetler, C. A., Kittaka, C., Rogers, R. R., Kuehn, R. E., and Liu, Z.: The CALIPSO automated aerosol classification and lidar ratio selection algorithm, J. Atmos. Ocean. Tech., 26, 1994–2014, https://doi.org/10.1175/2009JTECHA1231.1, 2009.

Ou-Yang, C. F., Lin, N. H., Sheu, G. R., Lee, C. T., and Wang, J. L.: Seasonal and diurnal variations of ozone at a high-altitude mountain baseline station in East Asia, Atmos. Environ., 46, 279–288, https://doi.org/10.1016/j.atmosenv.2011.09.060, 2012.

Ou-Yang, C. F., Ravindra Babu, S., Lee, J.-R., Yen, M.-C., Griffith, S. M., Lin, C.-C., Chang, S.-C., and Lin, N.-H.: Detection of stratospheric intrusion events and their role in ozone enhancement at a mountain background site in sub-tropical East Asia, Atmos. Environ., 268, 118779, https://doi.org/10.1016/j.atmosenv.2021.118779, 2022.

Pani, S. K., Ou-Yang, C.-F., Wang, S.-H., Ogren, J. A., Sheridan, P. J., Sheu, G.-R., and Lin, N.-H. J. A. E.: Relationship between long-range transported atmospheric black carbon and carbon monoxide at a high-altitude background station in East Asia, Atmos. Environ., 210, 86–99, https://doi.org/10.1016/j.atmosenv.2019.04.053, 2019.

Pani, S. K., Huang, H.-Y., Wang, S.-H., Holben, B. N., and Lin, N.-H.: Long-term observation of columnar aerosol optical properties over the remote South China Sea, Sci. Total Environ., 905, 167113, https://doi.org/10.1016/j.scitotenv.2023.167113, 2023.

Platnick, S., King, M., and Hubanks, P.: MODIS Atmosphere L3 Monthly Product, NASA MODIS Adaptive Processing System, Goddard Space Flight Center, USA, https://doi.org/10.5067/MODIS/MOD08_M3.006, 2015.

Raghuraman, S. P., Soden, B., Clement, A., Vecchi, G., Menemenlis, S., and Yang, W.: The 2023 global warming spike was driven by the El Niño–Southern Oscillation, Atmos. Chem. Phys., 24, 11275–11283, https://doi.org/10.5194/acp-24-11275-2024, 2024.

Ramanathan, V., Crutzen, P. J., Kiehl, J. T., and Rosenfeld, D.: Aerosols, climate, and the hydrological cycle, Science, 294, 2119–2124, https://doi.org/10.1126/science.1064034, 2001.

Ravindra Babu, S. and Lin, N.-H.: Changing pattern of springtime biomass-burning over Peninsular Southeast Asia (PSEA) in recent decades, ESS Open Archive, https://doi.org/10.22541/essoar.169111389.92212046/v2, 2023.

Ravindra Babu, S., Ou-Yang, C.-F., Griffith, S. M., Pani, S. K., Kong, S. S.-K., and Lin, N.-H.: Transport pathways of carbon monoxide from Indonesian fire pollution to a subtropical high-altitude mountain site in the western North Pacific, Atmos. Chem. Phys., 23, 4727–4740, https://doi.org/10.5194/acp-23-4727-2023, 2023.

Reid, J. S., Hyer, E. J., Johnson, R., Holben, B. N., Yokelson, R. J., Zhang, J., Campbell, J. R., Christopher, S. A., Di Girolamo, L., Giglio, L., Holz, R. E., Kearney, C., Miettinen, J., Reid, E. A., Turk, F. J., Wang, J., Xian, P., Zhao, G., Balasubramanian, R., Chew, B. N., Janai, S., Lagrosas, N., Lestari, P., Lin, N.-H., Mahmud, M., Nguyen, A. X., Norris, B., Oahn, N. T. K., Oo, M., Salinas, S. V., Welton, E. J., and Liew, S. C.: Observing and understanding the Southeast Asian aerosol system by remote sensing: An initial review and analysis for the Seven Southeast Asian Studies (7SEAS) program, Atmos. Res., 122, 403–468, https://doi.org/10.1016/j.atmosres.2012.06.005, 2013.

Sayer, A. M., Munchak, L. A., Hsu, N. C., Levy, R. C., Bettenhausen, C., and Jeong, M. J.: MODIS collection 6 aerosol products: comparison between Aqua's e-Deep Blue, Dark Target, and "merged" datasets, and usage recommendations, J. Geophys. Res.-Atmos., 119, 13965–13989, 2014.

Sheu, G.-R., Lin, N.-H., Wang, J.-L., Lee, C.-T., Ou Yang, C.-F., and Wang, S.-H.: Temporal distribution and potential sources of atmospheric mercury measured at a high-elevation background station in Taiwan, Atmos. Environ., 44, 2393–2400, https://doi.org/10.1016/j.atmosenv.2010.04.009, 2010.

Sinyuk, A., Holben, B. N., Eck, T. F., Giles, D. M., Slutsker, I., Korkin, S., Schafer, J. S., Smirnov, A., Sorokin, M., and Lyapustin, A.: The AERONET Version 3 aerosol retrieval algorithm, associated uncertainties and comparisons to Version 2, Atmos. Meas. Tech., 13, 3375–3411, https://doi.org/10.5194/amt-13-3375-2020, 2020.

Stein, A. F., Draxler, R. R., Rolph, G. D., Stunder, B. J. B., Cohen, M. D., and Ngan, F: NOAA's HYSPLIT atmospheric transport and dispersion modeling system, B. Am. Meteorol. Soc., 96, 2059–2077, https://doi.org/10.1175/BAMS-D-14-00110.1, 2015.

Tsay, S. C., Maring, H. B., Lin, N. H., Buntoung, S., Chantara, S., Chuang, H. C., Gabriel, P. M., Goodloe, C. S., Holben, B. N., Hsiao, T. C., Christina Hsu, N., Janjai, S., Lau, W. K. M., Lee, C. T., Lee, J., Loftus, A. M., Nguyen, A. X., Nguyen, C. M., Pani, S. K., Pantina, P., Sayer, A. M., Tao, W. K., Wang, S. H., Welton, E. J., Wiriya, W., and Yen, M. C.: Satellitesurface perspectives of air quality and aerosol-cloud effects on the environment: An overview of 7-SEAS/BASELInE, Aerosol Air Qual. Res., 16, 2581–2602, https://doi.org/10.4209/aaqr.2016.08.0350, 2016.

Twomey, S.: The Influence of Pollution on the Shortwave Albedo of Clouds, Journal of Atmospheric Sciences, 34, 1149–1152, https://doi.org/10.1175/1520-0469(1977)034<1149:TIOPOT>2.0.CO;2, 1977.

Vadrevu, K. P., Lasko, K., Giglio, L., Schroeder, W., Biswas, S., and Justice, C.: Trends in Vegetation fires in South and Southeast Asian Countries, Sci. Rep., 9, 7422, https://doi.org/10.1038/s41598-019-43940-x, 2019.

Wang, S., Cohen, J. B., Deng, W., Qin, K., and Guo, J.: Using a New Top-Down Constrained Emissions Inventory to Attribute the Previously Unknown Source of Extreme Aerosol Loadings Observed Annually in the Monsoon Asia Free Troposphere, Earths Fut., 9, e2021EF002167, https://doi.org/10.1029/2021EF002167, 2021.

Wang, S., Guan, L., Cohen, J. B., and Qin, K.: Reconstructing top-down global black carbon emissions using remote sensing and models, Atmos. Pollut. Res., 16, 102633, https://doi.org/10.1016/j.apr.2025.102633, 2025.

Warner, J., Carminati, F., Wei, Z., Lahoz, W., and Attié, J.-L.: Tropospheric carbon monoxide variability from AIRS under clear and cloudy conditions, Atmos. Chem. Phys., 13, 12469–12479, https://doi.org/10.5194/acp-13-12469-2013, 2013.

Warner, J. X., Comer, M. M., Barnet, C. D., McMillan, W. W., Wolf, W., Maddy, E., and Sachse, G.: A Comparison of Satellite Tropospheric Carbon Monoxide Measurements from AIRS and MOPITT During INTEX-A, J. Geophys. Res., 112, D12S17, https://doi.org/10.1029/2006JD007925, 2007.

Wei, J., Li, Z., Peng, Y., and Sun, L.: MODIS Collection 6.1 aerosol optical depth products over land and ocean: validation and comparison, Atmos. Environ., 201, 428–440, 2019a.

Wei, J., Li, Z., Sun, L., Peng, Y., and Wang, L.: Improved merge schemes for MODIS Collection 6.1 Dark Target and Deep Blue combined aerosol products, Atmos. Environ., 202, 315–327, 2019b.

Worden, H., Deeter, M., Edwards, D., Gille, J., Drummond, J., and Nédélec, P.: Observations of near-surface carbon monoxide from space using MOPITT multispectral retrievals, J. Geophys. Res.-Atmos., 115, D18314, https://doi.org/10.1029/2010JD014242, 2010.

Yin, S.: Biomass burning spatiotemporal variations over South and Southeast Asia, Environ. Int., 145, 106153, https://doi.org/10.1016/j.envint.2020.106153, 2020.

Yadav, I. C., Linthoingambi Devi, N., Li, J., Syed, J. H., Zhang, G., and Watanabe, H.: Biomass-burning in Indo-China peninsula and its impacts on regional air quality and global climate change – a review, Environ. Pollut., 227, 414–427, https://doi.org/10.1016/j.envpol.2017.04.085, 2017.

Zachariah, M., Vautard, R., Chaithra, S. T., Kimutai, J., Arulalan, T., AchutaRao, K., and Otto, F. E. L.: Extreme humid heat in South and Southeast Asia in April 2023, largely driven by climate change, detrimental to vulnerable and disadvantaged communities, World Weather Attribution, https://doi.org/10.25561/104092, 2023.

Zheng, H., Xue, L., Ding, K., Lou, S., Wang, Z., Ding, A., and Huang, X.: ENSO-Related Fire Weather Changes in Southeast and Equatorial Asia: A Quantitative Evaluation Using Fire Weather Index, J. Geophys. Res.-Atmos., 128, e2023JD039688, https://doi.org/10.1029/2023JD039688, 2023.

Zhu, A., Xu, H., Deng, J., Ma, J., and Li, S.: El Niño–Southern Oscillation (ENSO) effect on interannual variability in spring aerosols over East Asia, Atmos. Chem. Phys., 21, 5919–5933, https://doi.org/10.5194/acp-21-5919-2021, 2021.